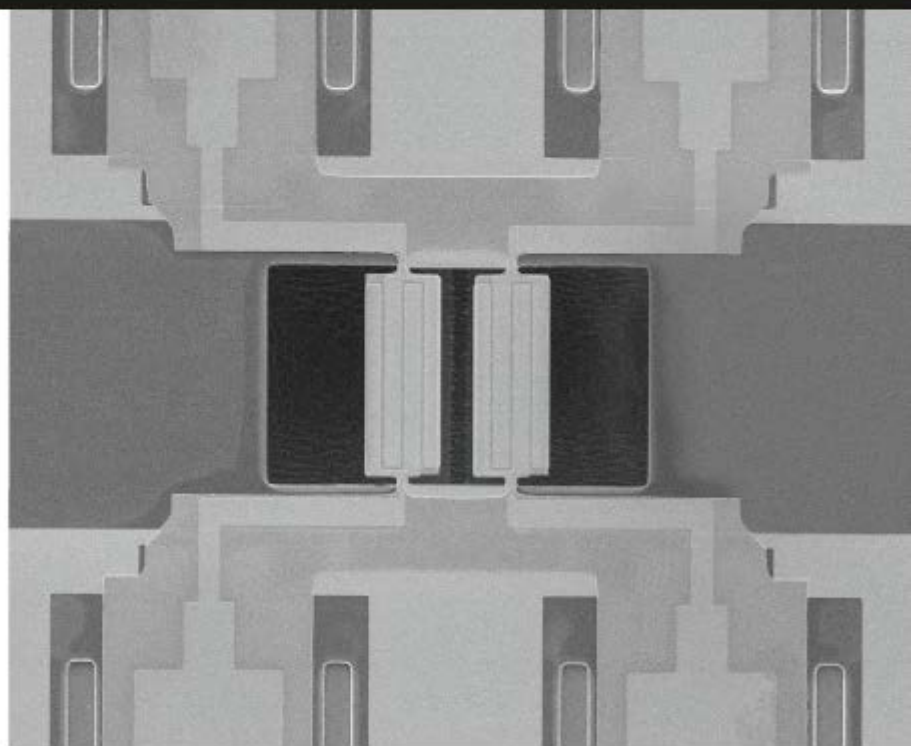


---

# PZT-on-Silicon RF-MEMS Lamb Wave Resonators and Filters



HADI YAGUBIZADE

PZT-ON-SILICON RF-MEMS  
LAMB WAVE RESONATORS AND  
FILTERS

Hadi Yagubizade

The Graduation Committee:

*Chairman and secretary:*

Prof. dr. ir. A.J. Mouthaan                      Universiteit Twente

*Promotor:*

Prof. dr. Miko C. Elwenspoek                      Universiteit Twente

*Assistant promotor:*

Dr. ir. Niels R. Tas                      Universiteit Twente

*Members:*

Prof. dr. D.J. Gravesteijn                      University of Twente

Prof. dr. ing. A.J.H.M. Rijnders                      University of Twente

Prof. dr. P.G. Steeneken                      Delft University of Technology

Dr. ir. H. Tilmans                      IMEC, Belgium

Dr. ir. R.J. Wiegerink                      University of Twente



This research is supported by the Dutch Technology Foundation STW, which is part of The Netherlands Organisation for Scientific Research (NWO) and partly funded by the Ministry of Economic Affairs (10048).



MESA<sup>+</sup> Institute for Nanotechnology  
P.O. Box 217, 7500 AE  
Enschede, The Netherlands

ISBN: 978-90-365-3594-6

DOI: <http://dx.doi.org/10.3990/1.9789036535946>

Cover:

Scanning Electron Micrograph of PZT-on-Silicon Band-Pass Filter (Chap. 5).  
Avrin Mountain, Khoy, West Azerbaijan, Iran.

This thesis was printed by Gildeprint Drukkerijen, The Netherlands  
Copyright © 2013 by Hadi Yagubizade, Enschede, The Netherlands  
All rights reserved. No part of this publication may be reproduced or stored in a retrieval system without the prior permission of the author.

Typeset with L<sup>A</sup>T<sub>E</sub>X.

# PZT-ON-SILICON RF-MEMS LAMB WAVE RESONATORS AND FILTERS

DISSERTATION

to obtain  
the degree of doctor at the University of Twente,  
on the authority of the rector magnificus,  
prof. dr. H. Brinksma,  
on account of the decision of the graduation committee  
to be publicly defended  
on Friday 13 December 2013 at 12:45

by

Hadi Yagubizade  
born on 3rd June 1982  
in Khoy, Iran

This dissertation has been approved by:

Promotor: Prof. dr. Miko C. Elwenspoek

Assistant Promotor: Dr. ir. Niels R. Tas

*To my parents, brother, and  
my wife*

# Contents

<b>1</b>	<b>Introduction</b>	<b>1</b>
1.1	Background and Motivation . . . . .	1
1.2	RF-MEMS Resonators and Filters . . . . .	2
1.3	Capacitive Transduction . . . . .	3
1.4	Piezoelectric Transduction . . . . .	4
1.4.1	One-/Two-Port Resonators . . . . .	5
1.4.2	RF-MEMS Bandpass Filters . . . . .	7
1.5	Thesis Outline . . . . .	8
<b>2</b>	<b>PZT-on-Silicon Length Extensional Mode Resonators</b>	<b>9</b>
2.1	Introduction . . . . .	9
2.2	Electrical Modeling . . . . .	10
2.3	Fabrication . . . . .	13
2.4	Conclusion . . . . .	18
<b>3</b>	<b>Higher-Order Longitudinal Mode PZT-on-Silicon Resonators</b>	<b>19</b>
3.1	Introduction . . . . .	20
3.2	Feed-Through Cancellation . . . . .	21
3.3	Fabrication . . . . .	22
3.4	Problem Formulation of Higher-Order Longitudinal Resonators . . . . .	23
3.4.1	Analytical Approach . . . . .	24
3.4.2	3D Finite-Element Eimulation . . . . .	26
3.5	Measurement Results and Discussion . . . . .	26
3.5.1	Set I: One Input and One Output Electrode (Symmetrical Configuration) . . . . .	27

3.5.2	Set II: Two-Input and One-Output Electrodes (Asymmetrical Configuration) . . . . .	32
3.5.3	Set III: Three-Input and Two-Output Electrodes (Asymmetrical Configuration) . . . . .	36
3.6	Conclusions . . . . .	37
<b>4</b>	<b>A Mechanically Coupled Contour Mode Bandpass Filter</b>	<b>41</b>
4.1	Introduction . . . . .	41
4.2	Fabrication And Characterization . . . . .	42
4.3	Conclusion . . . . .	45
<b>5</b>	<b>A 4th-Order Bandpass Filter Based on Differential Readout</b>	<b>49</b>
5.1	Introduction . . . . .	50
5.2	Concept And Simulation . . . . .	51
5.3	Characterization . . . . .	55
5.4	Conclusion . . . . .	61
<b>6</b>	<b>Conclusions</b>	<b>63</b>
6.1	Summary and Conclusion . . . . .	63
6.2	Original Contributions . . . . .	65
	<b>Bibliography</b>	<b>67</b>
	<b>Acknowledgement</b>	<b>77</b>
	<b>Samenvatting</b>	<b>79</b>
	<b>Abstract</b>	<b>83</b>
	<b>List of Publications</b>	<b>87</b>
	<b>Biography</b>	<b>89</b>

# Chapter 1

## Introduction

### 1.1 Background and Motivation

From early days of the electronic era, system designers have always depended on mechanically-vibrating elements (e.g., quartz crystals) for most of their frequency synthesis (oscillators) [1] and frequency selection (filters) [2] need. The unprecedented enhancement in the performance provided by these low-loss components have given them enough leverage to continue and extend their presence in electronic devices for many years.

Although the invention of the integrated circuits (IC) revolutionized the electronic industry, the need for off-chip quartz crystal and ceramic resonators has never been moderated. Integrated passives even though useful for some applications, are unacceptably lossy at higher frequencies. Therefore, demand for wireless communication devices operating at high frequencies promoted the application of discrete resonators further more. Meanwhile, piezoelectric vibrating components have evolved into new classes of devices such as surface acoustic wave (SAW) and bulk acoustic wave (BAW) resonators and filters with high operational frequencies. Novel micro-fabrication techniques developed for IC industry created opportunities for batch fabrication of these devices in smaller size and lower cost. However, they still consume far more area than the rest of the electronic circuit and can not be easily fabricated on the same substrate.

During the past several decades, the IC fabrication technology has matured to an extent that manufacturing a hand-held wireless device capable of communicating

voice, image, and digital information over multiple frequency bands is practically in reach. However, variety of resonators and filters required in these types of devices occupy a large percentage of the circuit board area and the manufacturing process is not cost effective. Therefore, the competition has already started for launching a technology, which enables implementation of all the required frequency-selective components on a single substrate that eventually will be integrated with the electronic circuit.

## 1.2 RF-MEMS Resonators and Filters

Quartz crystals and SAW devices are most used in wireless transceivers architectures [3, 4]. These devices show low input impedance and consequently low insertion loss (IL). This is the key reason of these devices to be irreplaceable for decades, even though they suffer from their large size and therefore, it is impossible to be on-chip integrated with the electronics.

The concept of MEMS resonators for the first time is presented using electrostatic actuation and readout mechanisms of a millimeter size resonant metal beam by the late 1960s [5]. Later on, by developing surface micromachining techniques, the concept of MEMS resonators is presented using polysilicon microstructures such as cantilever/clamped-clamped microbeams [6] and Comb-drives [7]. These devices provides a wide range of applications as sensing and actuating elements with high quality factor performance [8]. Their performance justifies additional fabrication processes which are required to make the device integrated in an electronic chip. However, flexural (bending mode) resonators were performing at lower resonance frequencies compared to SAW and quartz crystals. By boosting the resonance frequency, they are also suffering from thermo-elastic [9] and squeeze film [10, 11] dampings. To be able to boost the resonance frequency and still keeping the high quality factor of the resonators, miniaturized acoustic devices were presented. Thin-film bulk acoustic resonators (FBAR) [12] are the most successful MEMS resonators which are already commercialized. FBAR filters resonance frequency depend on the thickness of the thin-film and therefore is limited in the integration in a chip with multiple frequencies. To resolve this issue, acoustic Lamb wave (contour mode) MEMS resonators [13, 14] have been presented which have a resonance frequency which is lateral dimension dependent. These resonators have a high resonance frequency and still show a high quality performance as they are released from substrates and do not pene-

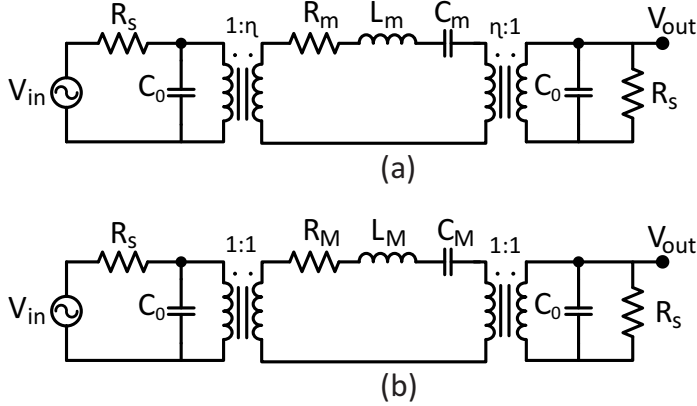


Figure 1.1: A 2-port resonator equivalent circuit, including the static capacitance of the resonator,  $C_0$  and the termination impedances,  $R_s$ , in (a) mechanical domain, and (b) electrical domain.

trates any solid wave (energy) to the substrate. These devices can be classified in two general categories: capacitive and piezoelectric resonators which are described in the following sections.

### 1.3 Capacitive Transduction

Capacitive resonators and filters are working based on electrostatic actuation and readout mechanisms of two parallel electrodes. There has been tremendous research on capacitive transduction resonators due to their compatibility with CMOS fabrication process and their high quality-factor [15, 16, 17, 18, 19, 20, 21, 22, 23, 24, 25, 26, 27, 28, 29, 30, 31, 32, 33, 34, 35, 36]. Disk resonators is most common configuration for these type of devices. However the devices are showing a high motional impedance and therefore a high insertion loss [13, 19]. The equivalent circuit of 2-port resonator is presented in Fig. 1.1. Fig. 1.1(a) and (b) shows the equivalent circuit of a resonator in mechanical (motional capacitance,  $C_m$ , inductance,  $L_m$ , and impedance,  $R_m$ ) and electrical domains (motional capacitance,  $C_M$ , inductance,  $L_M$ , and impedance,  $R_M$ ), respectively.  $\eta$  is the electro-mechanical coupling factor.  $\eta$ ,  $R_m$  and  $R_M$  in a capacitive transduction can be derived as follows:

$$\eta = V_{\text{dc}} \times \frac{\epsilon A}{g^2} \quad (1.1)$$

$$R_m = \frac{\sqrt{k \times m}}{Q} \quad (1.2)$$

$$R_M = \frac{\sqrt{k \times m}}{Q\eta^2} = \frac{\sqrt{k \times m}}{Q \times \left(\frac{V_{\text{dc}}\epsilon A}{g^2}\right)^2} \quad (1.3)$$

where  $k$  and  $m$  are the equivalent spring constant and mass of the resonator.  $Q$  is the quality factor,  $\epsilon$  is the dielectric constant of the material in the gap and  $A$  is the overlap area of the electrodes and  $g$  is the gap distance. As seen, to decrease the motional impedance of the resonator, the gap distance can be decreased and a DC-bias voltage ( $V_{\text{dc}}$ ) can be applied between the electrodes. Assuming  $R_M \gg R_s$ , it can be shown that the  $S_{21}$  of the resonator presented in Fig. 1.1 is:

$$S_{21}[\text{dB}] = -20 \log \left( 1 + \frac{R_m}{2R_s} \right) \quad (1.4)$$

Therefore, by decreasing the motional impedance,  $R_M$ , the insertion loss,  $S_{21}$ , will also decrease. Several attempts have been made to decrease the motional impedance of the capacitive resonators, e.g. filling the gap with high dielectric material [22, 32, 33, 34, 35, 36]. However, all these attempts did not lead to a low enough motional impedance. As seen in Eq. (1.4), another approach was increasing the termination resistance which shifts the  $S_{21}$  floor up, and will also reduce the insertion loss of the resonator, however this approach is limited to high frequencies due to the presence of parasitic capacitors.

## 1.4 Piezoelectric Transduction

Piezoelectric resonators consist of a piezoelectric layer with two thin-film metal layers. The electrical signal is applied to these metal layers and when the frequency of the electrical signal is equal to a certain resonance frequency of the resonator, that specific resonance mode will be excited. Unlike the capacitive resonators, piezoelectric devices do not have a switching voltage (DC-bias voltage), therefore the piezoelectric devices

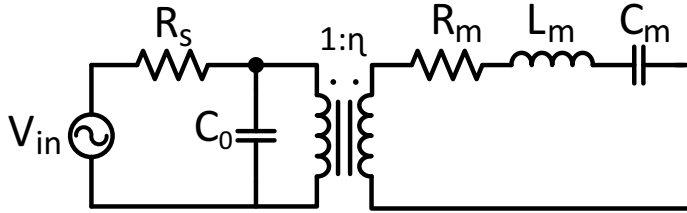


Figure 1.2: A equivalent circuit of a 1-port resonator.

are always active for all modes, therefore designing a specific dominant resonance mode (selective mode excitation) is a challenge. Lamb wave resonators can be designed as 1- or 2-port device. 1-port resonators are usually used for sensor applications and 2-port resonators are for both sensor [37, 38] and band-pass filter [39, 40, 41, 42] applications. These configuration are described in the following sections.

#### 1.4.1 One-/Two-Port Resonators

There are a lot of possible configuration for Lamb wave resonators [43, 44, 40, 45]. However, in this section we have presented few types of these configurations. In general, a 1-port Lamb wave piezoelectric resonator can be modeled as presented in Fig. 1.2. As seen, the resonator is actuated using an input signal and the output of the resonator is not loaded. These devices are usually used as sensor and characterized using their input impedance changes [37, 46]. The mechanical lumped parameters ( $R_m$ ,  $L_m$  and  $C_m$ ) and the electromechanical coupling coefficient ( $\eta$ ) are dependent on the configuration. The possible Lamb wave configurations of a 1-port piezoelectric resonator are presented in Fig. 1.3. Fig. 1.3(a) shows the case that the piezoelectric material is sandwiched between two metal layers and the first resonance frequency of the resonator depend on the length of the resonator ( $\lambda/2$ ). This case, is similar to FBAR resonators, however these type of Lamb wave resonators are released from the substrate and the resonator movement is perpendicular to the applied electric field. Therefore,  $e_{31}$  coefficient is the relevant piezoelectric property rather than  $e_{33}$  coefficient. Fig. 1.3(b) and (c) show two other possible configurations where the resonance frequency depends on the distance of the electrodes. Usually these configurations are utilized to actuate the resonators at higher resonance frequencies due to the shorter wavelength. Fig. 1.3(b) shows the case that the size of each electrode

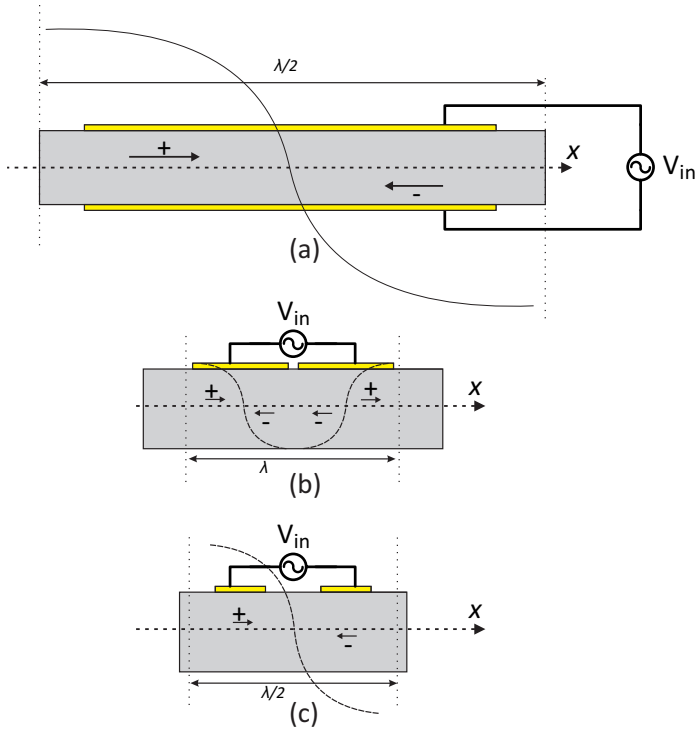


Figure 1.3: Three different 1-port resonator configurations.

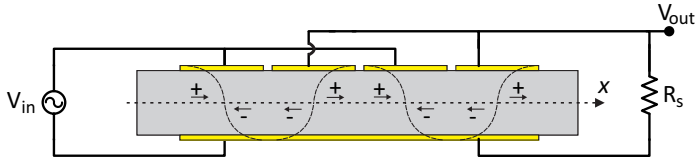


Figure 1.4: A conventional 2-port Lamb wave resonator configuration.

is equal to  $\lambda/2$  and Fig. 1.3(c) shows the case that the spacing is equal to the size of each electrode ( $\lambda/4$ ).

A conventional 2-port Lamb wave piezoelectric resonator is presented in Fig. 1.4. On one side of the piezoelectric layer, a set of input and output interdigitated electrodes and on the other side, a common grounding electrode is located. The input electrodes are contracting, the output electrodes in between the input electrodes, are expanding and vice versa. A 2-port resonator can also be modeled as in Fig. 1.1(b),

similar to the capacitive resonators. The electro-mechanical lumped parameters ( $R_M$ ,  $L_M$  and  $C_M$ ) and the electromechanical coupling coefficient ( $\eta$ ) depend on the configuration, however, for a specific configuration presented in Fig. 1.4, the equivalent motional impedance can be derived as [47, 48]:

$$R_M = \frac{\pi}{4N} \times \frac{\rho_{\text{PZT}}^{0.5} \times E_{\text{PZT}}^{0.5}}{Q} \times \frac{t}{L_e} \times \frac{1}{e_{31}^2}. \quad (1.5)$$

where  $N$  is the number of electrodes for each input and output assuming the number are the same for both ports,  $\rho_{\text{PZT}}$  is the density,  $E_{\text{PZT}}$  is the Young's modulus of the piezoelectric layer,  $Q$  is the quality factor,  $t$  is the thickness of the structure,  $L_e$  is the Length of resonator and  $e_{31}$  is the transverse piezoelectric coefficient.

### 1.4.2 RF-MEMS Bandpass Filters

SAW filters are a successful replacement of quartz crystal filters which have been commercialized for more than a decade. SAW devices are usually fabricated in single-crystalline piezoelectric substrates and are rather costly and not integrable due to their large off-chip size. FBAR filters are the latest generation of electro-mechanical filters used in wireless communication systems and its application is getting more and more dominant in cellphone market-share. In principle, FBAR filters can be integrated with CMOS IC processes using post-processing techniques, however, increasing the number of frequency bands for different applications is making this technology more expensive as its resonance frequency depends on the thickness. As a candidate for the next generation of bandpass filters, Lamb wave filters are getting more attention. However, they are still in the research stage and needs to be studied further to satisfy the demands of IC technology.

There are two main types of Lamb wave filters: mechanically [49, 50, 51] and electrically coupled filters [36, 52, 45]. In mechanically coupled filters, several Lamb wave resonators are coupled using a mechanical coupler and the stiffness of the coupler is determining the bandwidth of the filter. There are several challenges in utilizing Lamb wave filters. For example, in order to reduce the insertion loss of the filter at high frequencies, the wavelength of the corresponding frequency has to be rather small compared to the size of the resonators and therefore higher order resonators are utilized to increase the transduction area and reduce the insertion loss. Also the size of an optimum mechanical coupler also depends on the wavelength of the filter. Therefore, fulfilling all these criteria is a challenge.

## 1.5 Thesis Outline

In *chapter 2*, a 2-port length extension mode resonator is presented using a thin-film PZT layer. A feed-through cancellation method is proposed using bottom-electrode patterning and the performance enhancement is studied in the presence of a grounding resistance. Using this technique, a high stop-band rejection has been achieved compare to the conventional resonator configurations.

In *chapter 3*, 2-port higher-order longitudinal mode resonators are presented. 3D finite element simulation has been presented for each specific resonator and the effect feed-through cancellation has been studied using the simulation. The bottom-electrode and ground patterning techniques have been studied.

In *chapter 4*, a mechanically coupled bandpass filter is studied using two coupled contour mode resonators. The proposed filter is realized near 400 MHz. The resonators are actuated differentially and the filter output are differentially extracted. There is an improving in boosting the resonance frequency of PZT-based filters however, due to the existing feed-through at high frequencies, the rejection floor of the resonators was not improved.

In *chapter 5*, a 4th-order bandpass filter method based on differential readout of two in-phase actuated contour mode resonators with slightly different resonance frequencies is proposed. The proposed bandpass filter technique is realized at 400 MHz and 700 MHz. Using this technique, the feed-through signal is canceled and the stop-band rejection of the filter has been improved.

## Chapter 2

# PZT-on-Silicon Length Extensional Mode Resonators<sup>1</sup>

A length extensional mode lead zirconate titanate (PZT)-on-Si resonator is presented using  $50\ \Omega$  termination with high-stopband rejection exploiting feed-through cancellation. A 250 nm-thick (100)-dominant oriented PZT thin-film deposited on top of  $3\ \mu\text{m}$  Si using pulsed laser deposition (PLD) has been employed. The resonator is presented with the length of  $40\ \mu\text{m}$  (half-wavelength), which corresponds to a resonance frequency of about 83 MHz. The effect of feed-through cancellation has been studied to obtain high-stopband rejection using bottom electrode patterning in the presence of a specific grounding resistance. Using this technique, the stopband rejection can be improved by more than 20 dB.

### 2.1 Introduction

Nowadays, there is a great demand for integrated and reconfigurable RF bandpass filters to get rid of bulky, off-chip and expensive SAW filters and resonators, which can reduce the form factor, cost and increase the functionality of the next generation

---

<sup>1</sup>This chapter has been published in:

H. Yagubizade *et al.*, “Pulsed-Laser Deposited  $\text{Pb}(\text{Zr}_{0.52},\text{Ti}_{0.48})\text{O}_3$ -on-Silicon Resonators With High-Stopband Rejection Using Feed-Through Cancellation,” *Appl. Phys. Lett.* **102** 063509, 2013.

of wireless devices. Radio frequency MEMS (RF-MEMS) resonators are promising candidates for this purpose. Lamb-wave piezoelectric RF-MEMS resonators have demonstrated promising performance, such as low motional impedance and high  $Q$ -factor [53, 54, 55, 56, 57]. Their  $Q$ -factor has been boosted by integrating them with single crystalline materials, e.g. single-crystalline silicon [53, 54] and silicon carbide [55, 56], which store energy and deliver it back in each cycle with less loss compared to the piezoelectric medium. Also Lamb-wave resonators are of great interest for highly sensitive sensors due to their high  $Q$ -factor [57].

AlN, ZnO and recently PZT thin-films are the prevalent piezoelectric materials utilized in the resonators. Of these, PZT has the highest electromechanical coupling-factor. Also, the ferroelectric properties of PZT makes it more attractive for RF-MEMS applications. On the other hand, PZT has a lower phase velocity, which makes it difficult to achieve very-high resonance frequencies. However, higher composite phase velocities can be obtained by PZT in combination with other materials having higher phase velocities (e.g. silicon) [47]. Previously, PZT has been grown using chemical solution deposition methods [58] for RF-MEMS applications. In this chapter, a pulsed laser deposition (PLD) [59] has been exploited to grow a high-quality PZT thin-film with (100)-dominant orientation for RF-MEMS application. PZT suffers from a high feed-through due to its high dielectric permittivity and, as a consequence, drastically reduces the stopband rejection [60, 61]. In this chapter, we propose a feed-through cancellation method in the presence of specific grounding resistances (non-zero grounding) in input- and output-sides, which always exist and prevent the perfect grounding. Particularly, these grounding resistances have to be considered in the design of high-dielectric resonators, such as PZT.

In this chapter, a length extensional mode resonator, Fig. 2.1(a), with the length of  $40\ \mu\text{m}$  (half-wavelength) is presented. The basic configurations are presented in Fig. 2.1(b) and Fig. 2.1(c). The key aspects set forth in this chapter are the use of PLD-based PZT thin-film with its characteristics in RF-MEMS as well as presenting a feed-through cancellation method, which improves the stopband rejection by more than 20 dB.

## 2.2 Electrical Modeling

The effect of non-zero ground resistance  $R_g$  on the performance of a 2-port resonator with and without a patterned bottom-electrode is explored. An electrical

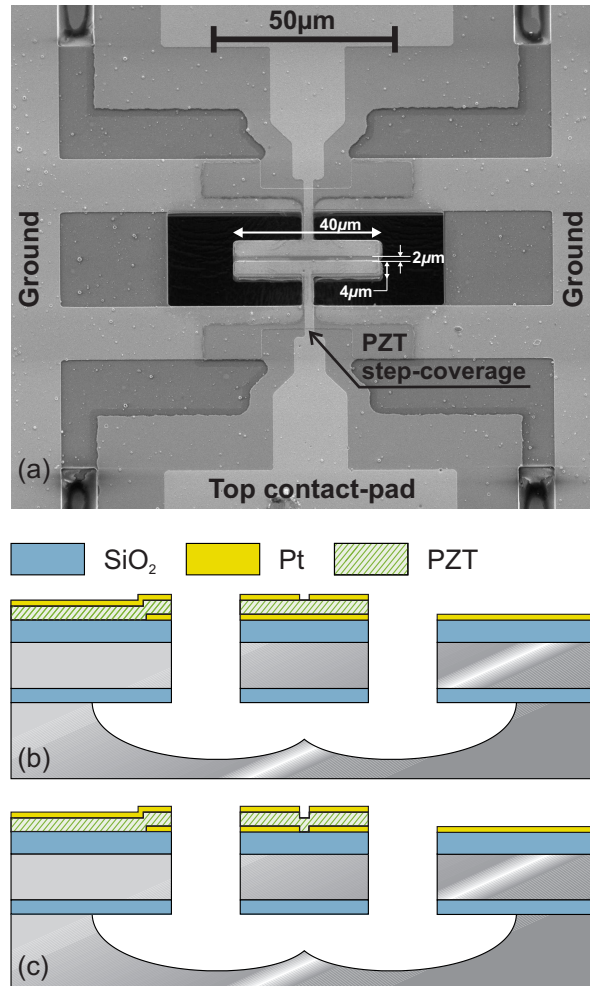


Figure 2.1: (a) Scanning electron micrograph (SEM) of a PZT-on-silicon resonator with the size of  $10 \times 40 \mu\text{m}^2$ . (b) The cross-section schematic of the un-patterned bottom-electrode device. (c) The cross-section schematic of the patterned bottom-electrode device.

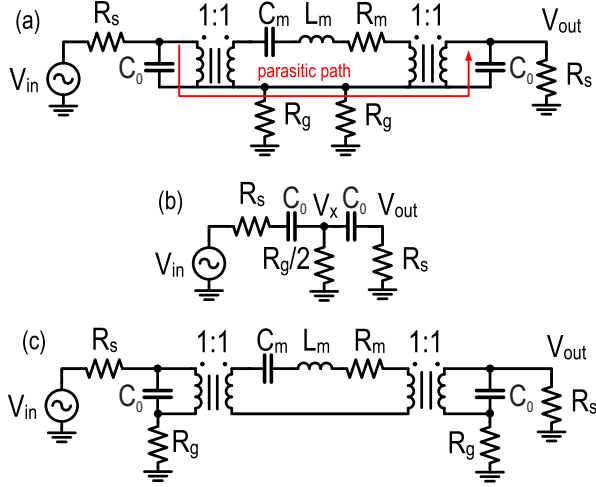


Figure 2.2: (a) A conventional 2-port resonator, including the static capacitance of the resonator,  $C_0$ , motional capacitance,  $C_m$ , inductance,  $L_m$ , and impedance,  $R_m$ , and the termination impedances,  $R_s$ . (b) Simplified model of the conventional 2-port resonator for frequencies outside the passband of the resonator (c) Splitting the ground of input- and output-ports to eliminate the parasitic path due to non-zero parasitic ground resistances,  $R_g$ .

model of a two-port resonator without bottom-electrode patterning is illustrated in Fig. 2.2(a) [60, 61]. The filter shown in Fig. 2.2(a) can be simplified to Fig. 2.2(b), because of the high impedance level of the resonator for frequencies out of its passband. The stopband gain of the resonator can be inferred from the circuit shown in Fig. 2.2(b). As  $R_g$  increases, the voltage gain at node  $V_x$  increases and as a consequence the rejection floor of the 2-port resonator can rise considerably and lower the stopband rejection to less than typically 5 dB. The stopband gain of the resonator  $A_{sb}$  in terms of  $r = R_g/R_s$  and  $\tau = R_s C_0$  can be described as:

$$A_{sb} = 20 \log \left( \frac{0.5r\tau^2\omega_0^2}{\sqrt{(1 - (1+r)\tau^2\omega_0^2)^2 + \tau^2\omega_0^2(2+r)^2}} \right) \quad (2.1)$$

The parasitic path in Fig. 2.2(a), is also responsible for the reduction of the passband gain of the resonator. By assuming that the source and load impedance are much lower than the motional impedance of the the resonator, Fig. 2.2(a) can be

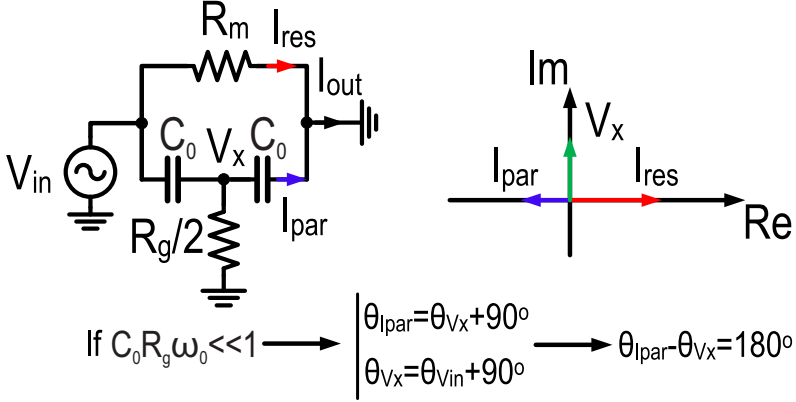


Figure 2.3: The simplified configuration of a conventional 2-port resonator at its resonance frequency.

simplified to Fig. 2.3 for frequencies around its resonance frequency. It can be shown that the current through the parasitic path has approximately  $180^\circ$  phase difference relative to the current through the resonator and consequently leads to a reduction in the total current delivered to the load resistance. The phase of  $V_x$  is approximately  $90^\circ$  larger than the phase of  $V_{in}$ , if  $C_0 R_g \omega_0 \ll 1$ , because of the highpass filtering between node  $V_x$  and  $V_{in}$ . Also, the phase of  $I_{par}$  is  $90^\circ$  larger than the phase of  $V_x$  and therefore,  $I_{par}$  is anti-phase with  $V_{in}$ . On the other hand,  $I_{res}$  is in-phase with  $V_{in}$ . Therefore,  $I_{res}$  and  $I_{par}$  will be anti-phase (see Fig. 2.3).

The effect of parasitic ground resistance on the transfer function of the resonator can be mitigated by splitting the ground connections of the input- and output-ports as shown in Fig. 2.2(c). As seen, the resonator is actuated by the voltage across  $C_0$  which is modified compared to the model presented by Pulskamp *et al.* [61]. In this way, the sensitivity of the transfer function of the filter to the non-zero ground resistance  $R_g$  will be drastically reduced. Using this technique, the parasitic path through the parasitic ground resistance will be eliminated.

## 2.3 Fabrication

The fabricated devices are shown in Fig. 2.1. In the 5-mask fabrication process, the bottom-electrode has been patterned before growing the PZT. The devices have been

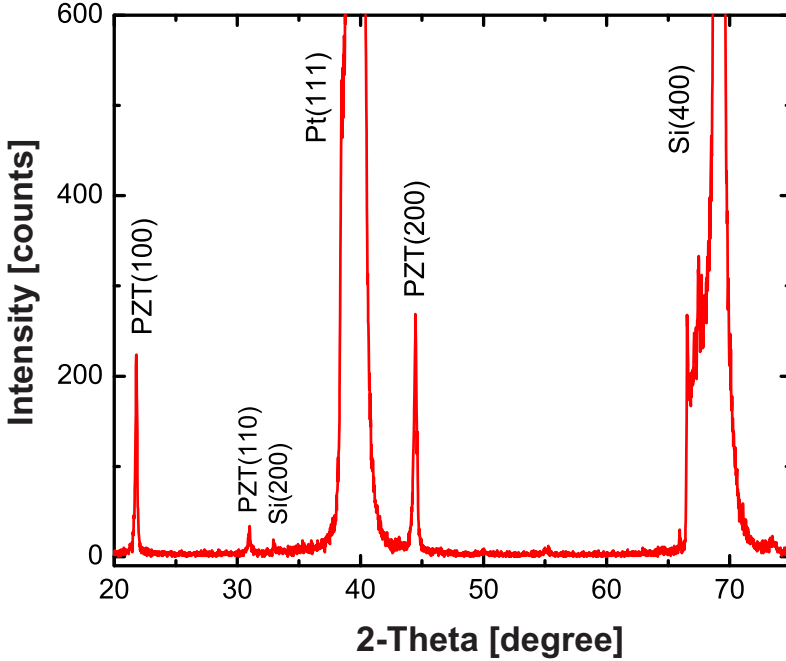


Figure 2.4: XRD pattern of PZT thin-films on Pt/Ti/SiO<sub>2</sub>/Si wafers.

fabricated in a 3  $\mu\text{m}$  silicon-on-insulator (SOI) wafer with 0.5  $\mu\text{m}$  buried oxide (BOX) layer. During the first step, a 670 nm silicon-oxide layer was grown. The thickness of this layer is chosen to compensate for the residual stresses of the other layers in the stack. 10/100 nm Ti/Pt has been sputtered and patterned using the first mask. A (100)-dominant thin-film (250 nm) PZT has been grown using PLD on LaNiO<sub>3</sub> as a seed layer. The crystalline structure of the PZT thin-films was measured using a Philips XPert X-ray diffractometer (XRD). A typical XRD pattern of the optimized PZT thin-films grown on 4-inch Pt/Ti/SiO<sub>2</sub>/Si wafers, using large-scale PLD, is given in Fig. 2.4. The films were prepared at 600  $^{\circ}\text{C}$  with an oxygen pressure of 0.1 mbar. The  $\theta$ - $2\theta$  scan clearly indicates the growth of PZT thin-films with (100)-preferred orientation and no pyrochlore phase is observed. On top of PZT, 100 nm thick Pt has been sputtered. Using the second mask, the top Pt layer has been patterned, followed by patterning PZT using a wet etchant (the third mask). Around the devices, an area has been opened by reactive ion etching (RIE) of the SiO<sub>2</sub>/Si/SiO<sub>2</sub> layer stack (fourth mask). Finally, using the fifth mask, the devices were released by isotropic etching of

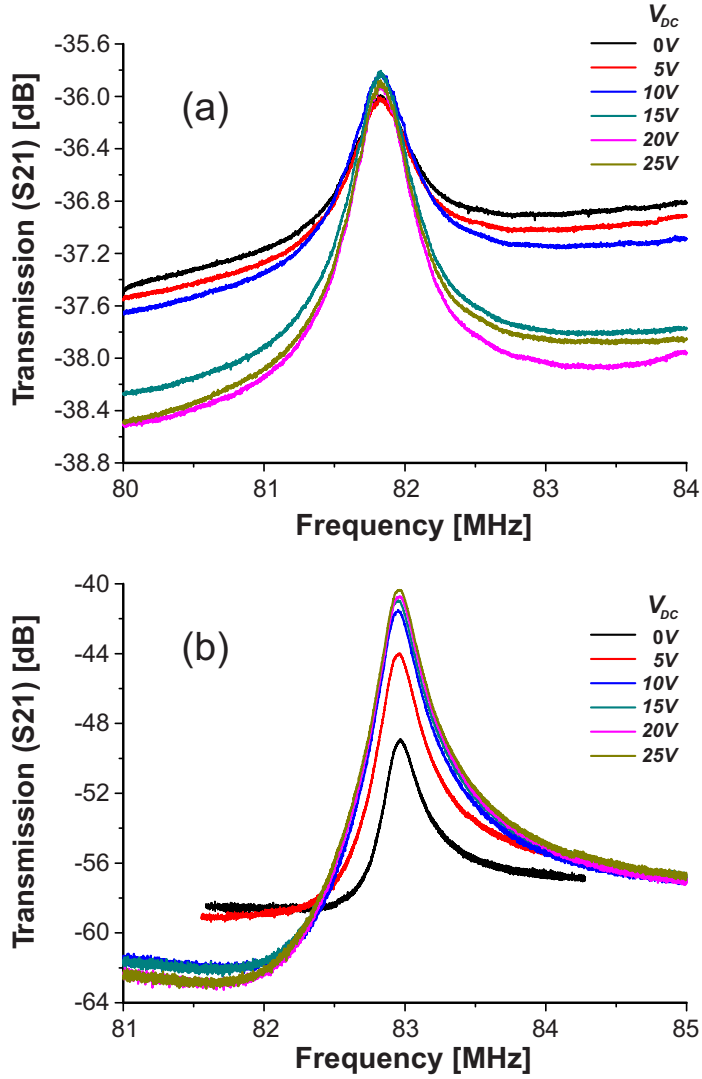


Figure 2.5: Measured transmission gain of resonators using  $50\ \Omega$  termination (a) with un-patterned bottom-electrode, (b) with patterned bottom-electrode.

Table 2.1: Material constants used in the calculations.

	Si<110>	SiO <sub>2</sub>	Pt	PZT
$E$ [GPa]	168.9	70	137.9	95.2
$\rho$ [Kg/m <sup>3</sup> ]	2329	2200	21090	7500
$\nu$	0.064	0.17	0.25	0.35

silicon, while the silicon device layer was protected by photoresist. In this fabrication process, the bottom Pt layer was etched under the top Pt contact-pads to minimize the parasitic capacitances. As seen in Fig. 2.1(a), PZT step-coverage has isolated the top and bottom Pt layers to prevent the shortcut.

The resonators were characterized in an RF probe station using Ground-Signal-Ground (GSG) probes. A Short-Open-Load-Thru (SOLT) calibration has been performed using impedance standard substrates (ISSs). All the measurements have been done by applying 0 dBm input power. The grounding resistances of all the measured devices are  $R_g \approx 5 \Omega$ . The frequency response of the fabricated devices for different DC-bias voltages are shown in Fig. 2.5. The DC-bias voltage has been applied both at the input- and output-ports using Bias-T's for all measurements. The frequency response of the un-patterned and patterned bottom-electrode, is shown in Fig. 2.5(a) and Fig. 2.5(b), respectively. It demonstrates clearly the effectiveness of bottom-electrode patterning on enhancing the stopband rejection. Thus, by utilizing this technique, the stopband rejection can be improved by more than 20 dB.

Table 2.2: The patterned bottom-electrode resonator's performance at different DC-bias voltages.

DC-bias[V]	$f_{\text{res}}$ [MHz]	$Q$ -factor	$C_m$ [fF]	$L_m$ [mH]	$R_m$ [k $\Omega$ ]	$e_{31}$ [C/m <sup>2</sup> ] <sup>a</sup>
0	82.9694	354	0.20	18.73	27.5	-1.420
5	82.9542	382	0.32	11.39	15.5	-1.821
10	82.9524	400	0.41	8.88	11.5	-2.062
15	82.9524	393	0.45	8.17	10.8	-2.150
20	82.9620	393	0.46	7.94	10.5	-2.181
25	82.9620	392	0.48	7.60	10.1	-2.229

<sup>a</sup> Other possible involved transductions, like capacitive, are neglected in these calculations.

The motional impedance of the resonator at different DC-bias voltages considering  $R_g$  as well as  $C_0$  has been extracted using Eq. (2.2), assuming that  $R_m \gg R_s$ .

$$S_{21}[\text{dB}] = -20 \log \left( 1 + (R_g + R_s)^2 C_0^2 \omega_0^2 \right) - 20 \log \left( 1 + \frac{R_g}{R_s} \right) - 20 \log \left( 1 + \frac{R_m}{2R_s} \right) \quad (2.2)$$

On the other hand, using the mechanical properties of a piezoelectric-transduced resonator, the motional impedance of the fundamental length extensional mode can be calculated as [53, 54, 47]

$$R_m = \frac{\pi \rho_{\text{eff}}^{0.5} E_{\text{eff}}^{0.5} t_{\text{total}}}{4 Q W} \frac{1}{e_{31}^2}. \quad (2.3)$$

In Eq. (2.3),  $t_{\text{total}}$  is the total device composite stack thickness ( $t_{\text{total}} = t_{\text{BOX}} + t_{\text{Si}} + t_{\text{SiO}_2} + t_{\text{Pt, bottom}} + t_{\text{PZT}} + t_{\text{Pt, top}}$ ). The width of each input- and output-electrode is  $W_e = 4 \mu\text{m}$  with  $2 \mu\text{m}$  spacing in between, illustrated in Fig. 2.1(a). The total width of the resonator is  $W = 10 \mu\text{m}$ . The values for the Young's moduli ( $E_i$ ), densities ( $\rho_i$ ) and Poisson's ratios ( $\nu_i$ ) are listed in Table 2.1 [62].

By comparing the measured (Eq. (2.2)) and calculated (Eq. (2.3)) motional impedances, the transverse piezoelectric coefficient ( $e_{31}$ ) of 250 nm-thick PZT have been extracted at different DC-bias voltages and listed in Table 2.2. It is illustrated that the absolute value of the  $e_{31}$  increased from 1.420 to 2.229 C/m<sup>2</sup> with DC-bias voltage in the range of 0-25 V. The variation of the  $e_{31}$  with the DC-bias voltage is associated with the piezoelectric domain re-orientation process. At low DC-bias voltages (0-10 V), the main contribution to the  $e_{31}$  is due to the increase in the domain reversal with increasing DC-bias voltage. At higher DC-bias voltages (15-25 V), most switchable domains have already been aligned along the direction of the DC-bias voltage, the  $e_{31}$  variation is smaller since it is determined mainly by the variations of the dipoles[63].

By applying the DC-bias voltage, the motional impedance is decreasing due to the enhancement of the transverse piezoelectric coefficient. Therefore, as seen in Fig. 2.5(b), by applying the DC-bias voltage, the passband gain of the resonator increases. The motional capacitance ( $C_m$ ) and inductance ( $L_m$ ) have been extracted and reported in Table 2.2.

At higher DC-bias voltages, the resonator's efficiency increases, but the corresponding increase in effective Young's modulus will lead to a shift in resonance frequency. As the PZT thin-film fabricated in this chapter is only 250 nm thick, the shift in resonance frequency is considerably lower than the one in previous designs [53], leading to a measured frequency shift of only 0.03%.

## 2.4 Conclusion

In conclusion, we demonstrated a feed-through cancellation method to improve the stopband rejection of PZT-on-Si resonator based on bottom-electrode patterning only. We have used a high-quality PLD-based PZT thin-film. Using the proposed technique, the stopband rejection of the resonator has been improved by more than 20 dB.

## Chapter 3

# Higher-Order Longitudinal Mode PZT-on-Silicon Resonators<sup>1</sup>

Higher-order longitudinal mode resonators are presented using 500 nm-thick pulsed-laser deposited (PLD) lead zirconate titanate (PZT) on top of 3  $\mu\text{m}$  silicon (PZT-on-Silicon). Three sets of resonators, Set I, Set II and Set III, are presented with 1-,  $1\frac{1}{2}$ - and  $2\frac{1}{2}$ -wavelength, respectively. The resonators are presented at a resonance frequency around 75 MHz with 44  $\mu\text{m}$  wavelength. The 2-port resonators are characterized using 50  $\Omega$  termination. The effect of bottom-electrode and ground-patterning on feed-through cancellation have been studied. The bottom-electrode patterning means splitting the input and output ground electrodes inside the device underneath the PZT layer and ground patterning means splitting the ground outside the device. Each three sets contain four different cases, 1. not bottom-electrode and not ground patterned, 2. bottom-electrode patterned and not ground patterned, 3. not bottom-electrode patterned and ground patterned, and 4. both bottom-electrode and ground patterned. The bottom-electrode and ground patternings shows an effective approach for feed-through cancellation and increasing the stopband rejection. A comprehensive finite-element analysis using fully-coupled electrical and mechanical

---

<sup>1</sup>This chapter has been submitted to

H. Yagubizade *et al.*, “Higher-Order Longitudinal Mode PZT-on-Silicon Resonators: Bottom-Electrode and Ground Patterning,” *J. Micromechanics and Microengineering*, 2013.

domains as well as an analytical analysis have been performed to study and simulate the transmissions of the resonators.

### 3.1 Introduction

High-frequency acoustic micro-electro-mechanical system (MEMS) or RF-MEMS resonators are showing promising performance for next generation of miniaturized and integrated systems. Various applications such as radio frequency (RF) oscillators [14] and filters [50, 51, 64], optomechanical systems [65], electrical transformers [66, 67, 68] are shaping up using these systems. Lamb-wave RF-MEMS resonators have demonstrated promising performance, such as high quality-factor ( $Q$ -factor) due to the released structures, higher phase velocity and smaller size compared to the traditional acoustic resonators means SAW resonators. Lamb-wave resonators are still in the perfecting state and therefore there is a great demand for further understanding of various issues such as reducing the anchor-loss [69], spurious modes suppression using various designs and simulation techniques such as finite-element methods.

Electrostatic [13], piezoelectric [70, 53, 54, 55, 56, 47, 58] and capacitive-piezoelectric [71] are most exploited transduction techniques in Lamb-wave devices. The capacitive transduction-based devices stands up for their excellent  $Q$ -factors but suffer from high motional impedance. The piezoelectric devices show lower motional impedance but suffers from lower  $Q$ -factor. Recently a combined technique means capacitive-piezo devices show up as a candidate for Lamb-wave devices but still shows higher insertion loss compared to the pure piezoelectric transduction.

The  $Q$ -factor of piezoelectric Lamb-wave resonators has been boosted by integrating them with single crystalline materials, e.g. single-crystalline silicon [53, 54] and silicon carbide [55, 56], which store energy and deliver it back in each cycle with less loss compared to the piezoelectric medium.

AlN, ZnO and recently PZT thin-films are the prevalent piezoelectric materials utilized in the resonators. Of these, PZT has the highest electro-mechanical coupling-factor. Also, the ferroelectric properties of PZT makes it more attractive for RF-MEMS applications. On the other hand, PZT has a lower phase velocity, which makes it difficult to achieve very-high resonance frequencies. However, higher composite phase velocities can be obtained by PZT in combination with other materials having higher phase velocities (e.g. silicon) [47]. Previously, PZT has been grown using chemical solution deposition methods [58, 72] for RF-MEMS applications. In this

chapter, a pulsed laser deposition (PLD) [48, 59] has been exploited to grow a high-quality PZT thin-film with (100)-dominant orientation for RF-MEMS application. PZT suffers from a high feed-through due to its high dielectric permittivity and, as a consequence, drastically reduces the stopband rejection [48, 60, 61].

Recently, a new method has been presented called feed-through cancellation method [48, 60, 61]. Feed-through cancellation is an irrefutable fact due to not perfect grounding in nature caused by the presence of specific grounding resistances (non-zero grounding) in input- and output-port. Particularly, these grounding resistances have to be considered in the design of high-dielectric resonators, such as PZT. This technique is realized by patterning the bottom-electrode before growing the PZT layer on top of that.

In this chapter, the feed-through cancellation technique has been studied in higher-order longitudinal mode resonators in more detail. This technique has been investigated further by studying the effect of ground splitting technique between input- and output-ports outside the device. Therefore, four different case studies have been studied as: 1. not bottom-electrode and not ground patterned, 2. bottom-electrode patterned and not ground patterned, 3. not bottom-electrode patterned and ground patterned, and 4. both bottom-electrode and ground patterned. A comprehensive finite-element analysis using COMSOL Multiphysics<sup>®</sup> with fully-coupled electrical and mechanical domains as well as an analytical analysis have been performed to study and simulate the transmissions of the resonators.

## 3.2 Feed-Through Cancellation

PZT-transduced devices suffer from high feed-through due to their high dielectric permittivity. In this section, we discuss this issue and its relation with grounding resistance and how this issue can be solved using techniques called bottom-electrode as well as ground patterning. In this chapter we study three sets of longitudinal devices at around 75 MHz. The first set (Set I), consists of a full-wavelength containing of a half-wavelength for input and a half-wavelength for output electrodes. This set has a symmetrical configuration for input- and output-ports. The second and third sets (Set II and Set III), have asymmetrical configurations. Set II consists of two input and one output electrode and Set III consists of three input and two output electrodes. The length of input and output electrodes as well as the spacing between the electrodes are fixed to 40  $\mu\text{m}$  and 4  $\mu\text{m}$  in all the devices, respectively. Therefore

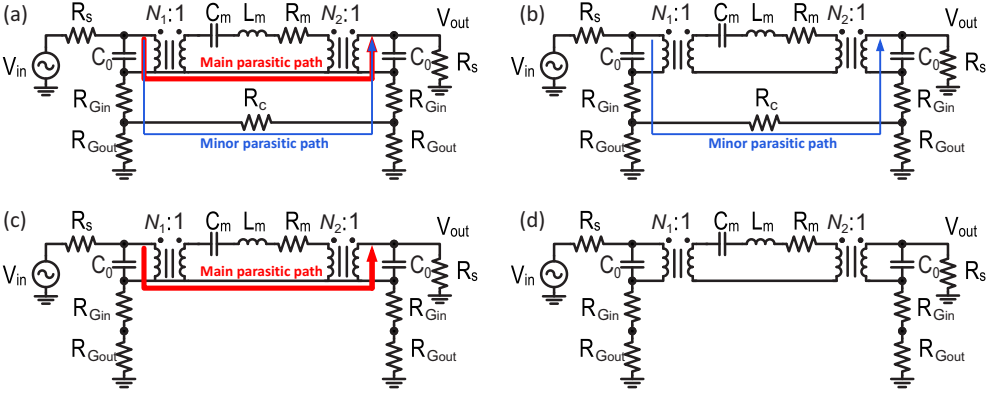


Figure 3.1: 2-port resonator models, including the static capacitance of the resonator,  $C_0$ , motional capacitance,  $C_m$ , inductance,  $L_m$ , and impedance,  $R_m$ , and the termination impedances,  $R_s$ . with configurations of (a) un-patterned bottom-electrode and ground, (b) patterned bottom-electrode and un-patterned ground, (c) un-patterned bottom-electrode and patterned ground, and (d) patterned bottom-electrode and ground.

by increasing the length of the resonators and consequently the number of electrodes, the resonance frequency of the devices are slightly decreasing due to the increase of the number of the spacings and therefore the wavelength of the resonators. Each set contains four different types of the configurations depicted in Fig. 3.1. The first device (Type (a)) is with not-patterned bottom-electrode and not-patterned ground configuration, Fig. 3.1(a). The second device (Type (b)) is with patterned bottom-electrode and not-patterned ground configuration, Fig. 3.1(b). The third device (Type (c)) is with not-patterned bottom-electrode and patterned ground configuration, Fig. 3.1(c). The last device (Type (d)) is with patterned bottom-electrode and patterned ground configuration, Fig. 3.1(d).

### 3.3 Fabrication

The devices were fabricated with five masks on a  $3\ \mu\text{m}$  silicon-on-insulator (SOI) wafer with  $0.5\ \mu\text{m}$  buried oxide (BOX) layer, Fig. 3.2. The fabrication started with oxidizing the silicon device layer for  $680\ \text{nm}$ . The thickness of this layer is chosen to

compensate the residual stresses of the composite structure. 10/100 nm Ti/Pt has been sputtered and patterned using the first mask, Fig. 3.2(a). A (100)-dominant thin-film (500 nm) PZT has been grown using PLD on  $\text{LaNiO}_3$  as a seed layer. The crystalline structure of the PZT thin-films was measured using a Philips XPert X-ray diffractometer (XRD). A typical XRD pattern of the optimized PZT thin-films grown on 4-inch Pt/Ti/SiO<sub>2</sub>/Si wafers, using large-scale PLD, is given in Fig. 3.3. The films were prepared at 600 °C with an oxygen pressure of 0.1 mbar. The  $\theta$ - $2\theta$  scan clearly indicates the growth of PZT thin-films with (100)-preferred orientation and no pyrochlore phase is observed.

On top of PZT, 100 nm thick Pt has been sputtered, Fig. 3.2(b). Using the second mask, the top Pt layer has been patterned, Fig. 3.2(c). After, the PZT was patterned using a wet etchant (the third mask), Fig. 3.2(d). The device boundaries, the area that defines the device and the anchors were patterned by reactive ion etching (RIE) of the SiO<sub>2</sub>/Si/SiO<sub>2</sub> layer stack (fourth mask), Fig. 3.2(e). Before releasing the devices, the silicon device layer (side walls) were covered and protected using a planarized photoresist (fifth mask), Fig. 3.2(f). Finally, the devices were released by isotropic etching of silicon, while the silicon device layer was protected by photoresist. In this fabrication process, the bottom Pt layer was etched under the top Pt contact-pads to minimize the parasitic capacitances. As seen in Fig. 3.2, PZT step-coverage has isolated the top and bottom Pt layers to prevent the shortcut.

## 3.4 Problem Formulation of Higher-Order Longitudinal Resonators

In this section, first we present analytical formulas to study the motional impedance, -capacitance and -inductance of the resonators. Using the analytical approach, the piezoelectric coefficient is extracted. Later, using the extracted piezoelectric coefficient, a finite-element simulation is performed with a fully electro-mechanical coupled approach using COMSOL Multiphysics<sup>®</sup>. This approach gives the opportunity for further designing and studying the resonators/filters and possibly to improve the designs.

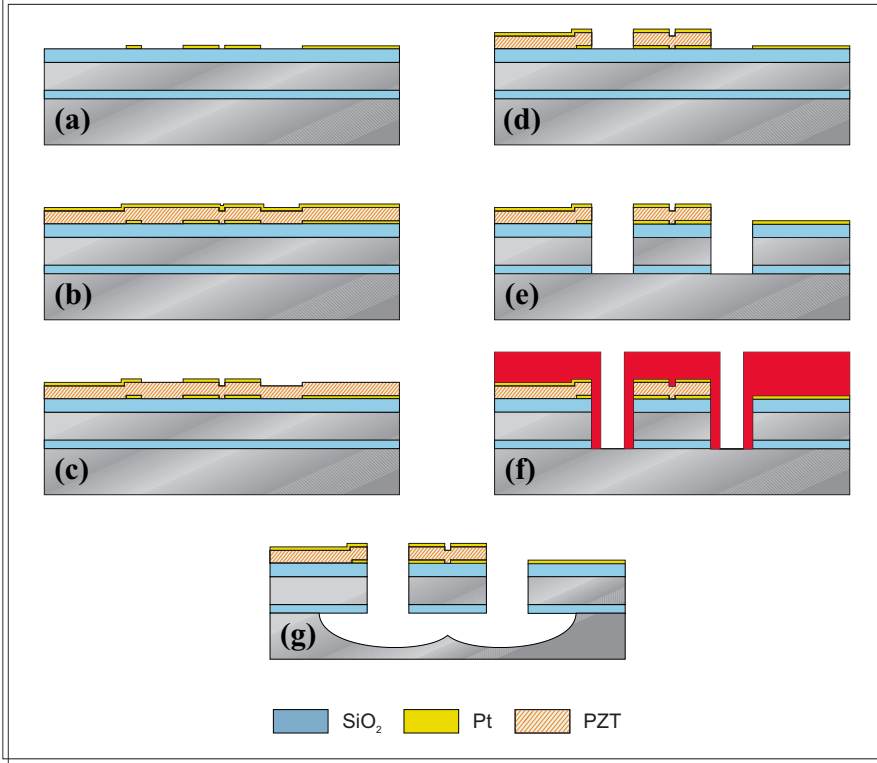


Figure 3.2: The fabrication process flow of PZT-on-Silicon resonators.

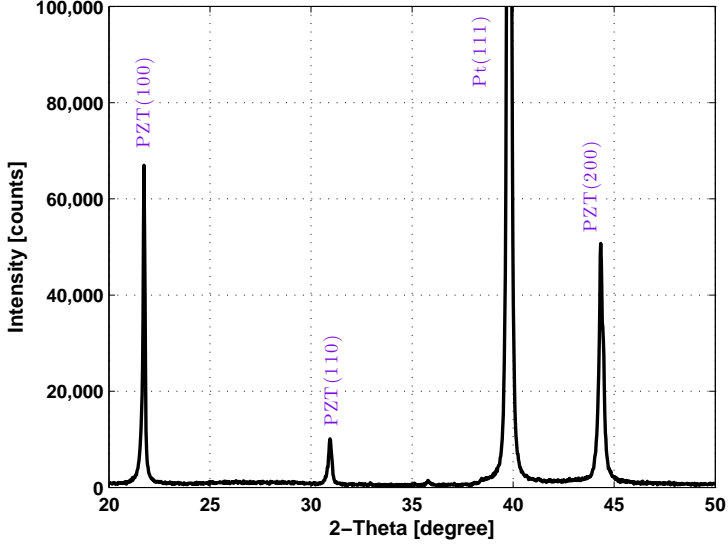
### 3.4.1 Analytical Approach

For a higher-order resonator, the input and output electro-mechanical coupling coefficients ( $\eta_1$  and  $\eta_2$ ) are defined as,

$$\eta_1 = N_1 (2e_{31}w_{e1}), \eta_2 = N_2 (2e_{31}w_{e2}), \quad (3.1)$$

where  $N_1$  and  $N_2$  are the input and output coupling coefficients,  $w_{e1}$  and  $w_{e2}$  are the width of each input- and output-electrodes, and  $e_{31}$  is the transverse piezoelectric coefficient.

Using the mechanical properties of a piezoelectric-transduced resonator, it can be shown that the equivalent motional impedance, -capacitance and -inductance of


 Figure 3.3: XRD pattern of PZT thin-film on Pt/Ti/SiO<sub>2</sub>/Si wafers.

longitudinal mode resonator with  $w_e = w_{e1} = w_{e2}$ , can be calculated as [54, 47]

$$R_m = \frac{\pi}{2\Gamma} \frac{\rho_{\text{eff}}^{0.5} E_{\text{eff}}^{0.5} t_{\text{total}}}{Q} \frac{1}{w_e e_{31}^2}, \quad (3.2)$$

$$C_m = \frac{2\Gamma}{\pi^2} \frac{w_e L}{t_{\text{total}} E_{\text{eff}}} \frac{1}{e_{31}^2}, \quad (3.3)$$

$$L_m = \frac{1}{2\Gamma} \frac{L t_{\text{total}} \rho_{\text{eff}}}{w_e} \frac{1}{e_{31}^2}. \quad (3.4)$$

where assuming  $n = N_1 + N_2$ ,  $\Gamma = n$  for even  $n$  (symmetric resonator) and  $\Gamma = (n^2 - 1)/n$  for odd  $n$  (asymmetric resonator).

In Eq. (3.3),  $t_{\text{total}}$  is the total device composite stack thickness ( $t_{\text{total}} = t_{\text{BOX}} + t_{\text{Si}} + t_{\text{SiO}_2} + t_{\text{Pt, bottom}} + t_{\text{PZT}} + t_{\text{Pt, top}}$ ).  $Q$  is the quality factor of the resonator.

On the other hand, the motional impedance of the resonator at different DC-bias voltages considering  $R_g$  as well as  $C_0$  has been extracted using Eq. (3.2), assuming that  $R_m \gg R_s$ .

$$\begin{aligned}
 S_{21}[\text{dB}] = & -20 \log \left( 1 + (R_g + R_s)^2 C_0^2 \omega_0^2 \right) \\
 & -20 \log \left( 1 + \frac{R_g}{R_s} \right) - 20 \log \left( 1 + \frac{R_m}{2R_s} \right)
 \end{aligned} \tag{3.5}$$

By comparing the measured (Eq. (3.2)) and calculated (Eq. (3.3)) motional impedances, the transverse piezoelectric coefficient ( $e_{31}$ ) of the PZT layer can be extracted at resonance frequencies.

### 3.4.2 3D Finite-Element Emulation

For finite-element simulation, COMSOL Multiphysics<sup>®</sup> version 4.3a has been used. For this simulation, Piezoelectric Devices (pzd) and Electrical Circuit (cir) physics are fully coupled. Inside the pzd-physics, two domains have been considered for isotropic and anisotropic layers means silicon oxide and silicon respectively. In this simulation, the Pt layers are neglected. The fixed constraint boundary condition has been applied at the end-side of the anchors. Isotropic loss factors are set at each domain based on the measured  $Q$ -factor. The bottom-electrodes are selected as ground inside the pzd-physics and top electrodes are selected as terminal 1 and 2 as input and output ports to be connected to the cir-physics. In cir-physics, all the four case studies depicted in Fig. 3.1 can be simulated at cir-physics. For both input and output sides  $50 \Omega$  termination resistances have been used. The actuation has been done using the cir-physics. The fully coupled solver has been employed in the study. The output voltage across the termination resistance is used to extract the  $S_{21}$ -parameter of the resonators.

## 3.5 Measurement Results and Discussion

The resonators were characterized in an RF probe station using Ground-Signal-Ground (GSG) probes. A Short-Open-Load-Thru (SOLT) calibration has been performed using a impedance standard substrate (ISS). The DC-bias voltage has been

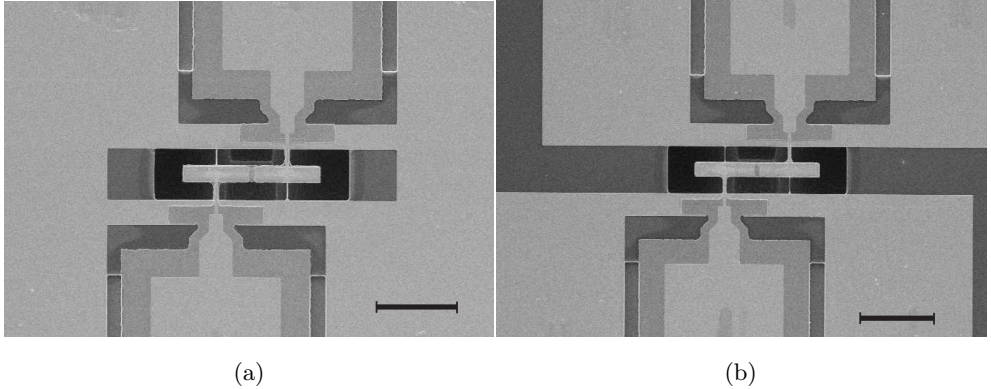


Figure 3.4: Scanning electron micrograph (SEM) of a PZT-on-silicon resonator (one-input and one-output electrode) with (a) un-patterned ground, and (b) patterned ground, (Scale bar 50  $\mu\text{m}$ ).

applied both at the input- and output-ports using Bias-T's for all measurements. All the measurements have been done at 0 dBm input power.

### 3.5.1 Set I: One Input and One Output Electrode (Symmetrical Configuration)

The frequency response of Set I devices (Fig. 3.4) for different DC-bias voltages are shown in Fig. 3.5. The sequences in Fig. 3.5 are based on Fig. 3.1. Thus, Fig. 3.5(a) shows the frequency response of the un-patterned bottom-electrode and ground, Fig. 3.5(b) shows the patterned bottom-electrode and un-patterned ground, Fig. 3.5(c) shows the un-patterned bottom-electrode and patterned ground, and Fig. 3.5(d) shows the patterned bottom-electrode and ground. As seen in Fig. 3.5(a)

Table 3.1: Material constants used in the calculations.

	Si<110>	SiO <sub>2</sub>	Pt	PZT
$E$ [GPa]	168.9	70	137.9	95.2
$\rho$ [Kg/m <sup>3</sup> ]	2329	2200	21090	7500
$\nu$	0.064	0.17	0.25	0.35

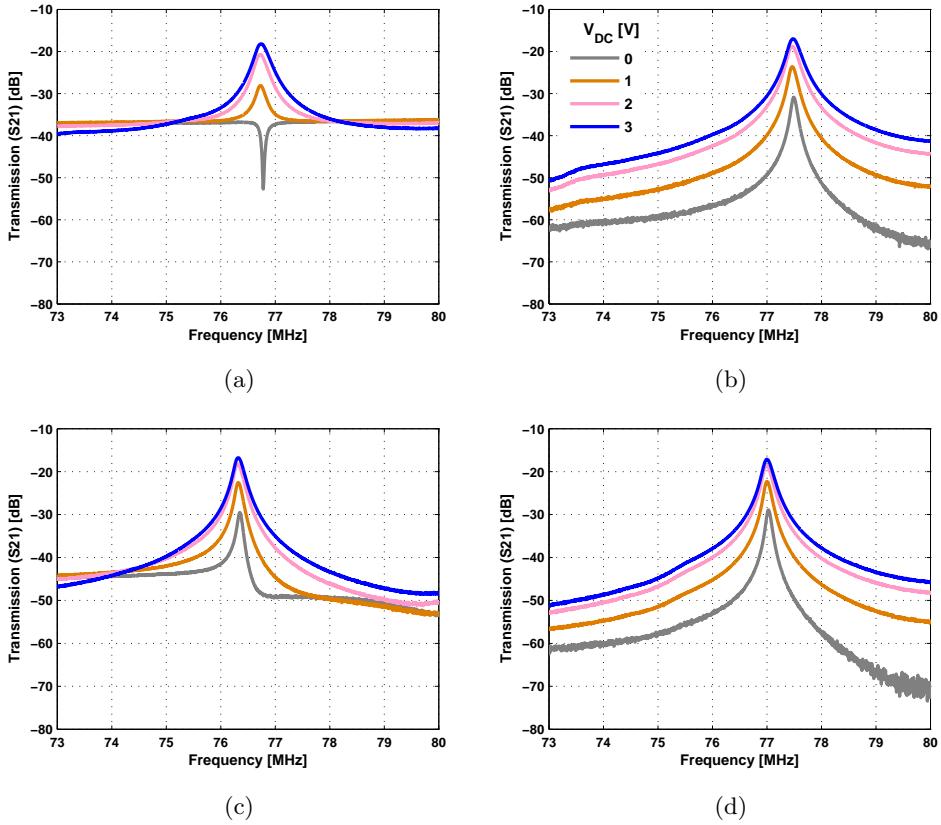


Figure 3.5: Measured transmission of Set I resonators using  $50\ \Omega$  termination with (a) un-patterned bottom-electrode and ground, (b) patterned bottom-electrode and un-patterned ground, (c) un-patterned bottom-electrode and patterned ground and (d) patterned bottom-electrode and ground.

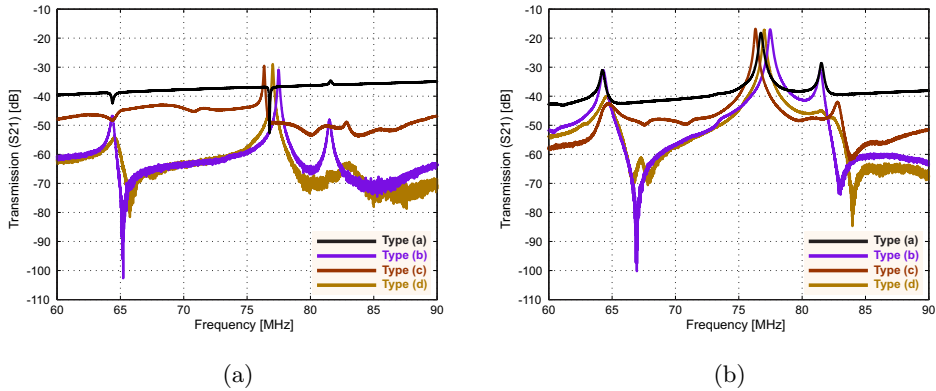


Figure 3.6: Measured frequency response of Set I resonators with four different electrode patternings (a) without DC-bias voltage and (b) DC-bias voltage of 3V

and (b), patterning the bottom-electrode improves the stopband rejection around 20 dB at DC-bias voltage of 0 V and around 10 dB at DC-bias voltage of 3 V. As seen in Fig. 3.5(a) and (b) at DC-bias voltage of 0 V, the response turns from stopband response to passband response. As shown in Fig. 3.5(b) and (d), by patterning the bottom-electrode the responses become very similar and therefore by patterning the bottom-electrode, the most dominant feed-through signal has been canceled. By comparing Fig. 3.5(c) and (a), the stopband rejection has been improved but is lower than the stopband rejection of Type(b) and (d). If in the fabrication, patterning of the bottom-electrode is not possible, therefore only patterning of the ground could improve the response.

For further comparison, the transmission responses of four types of the devices with wider frequency range are presented in Fig. 3.6(a) and (b) with DC-bias voltages of 0 V and 3 V, respectively.

For analyzing the responses, the analytical and the finite-element simulations described previously, are implemented. The values for the Young's moduli ( $E_i$ ), densities ( $\rho_i$ ) and Poisson's ratios ( $\nu_i$ ) are listed in Table 3.1 [62]. As a case study, the devices of Type(a) and (b), at DC-bias voltage of 3 V are analyzed. The motional impedances are calculated using Eq. (3.5) and by comparing with Eq. (3.2), the  $e_{31}$  has been extracted at different DC-bias voltages and listed in Table 3.2.

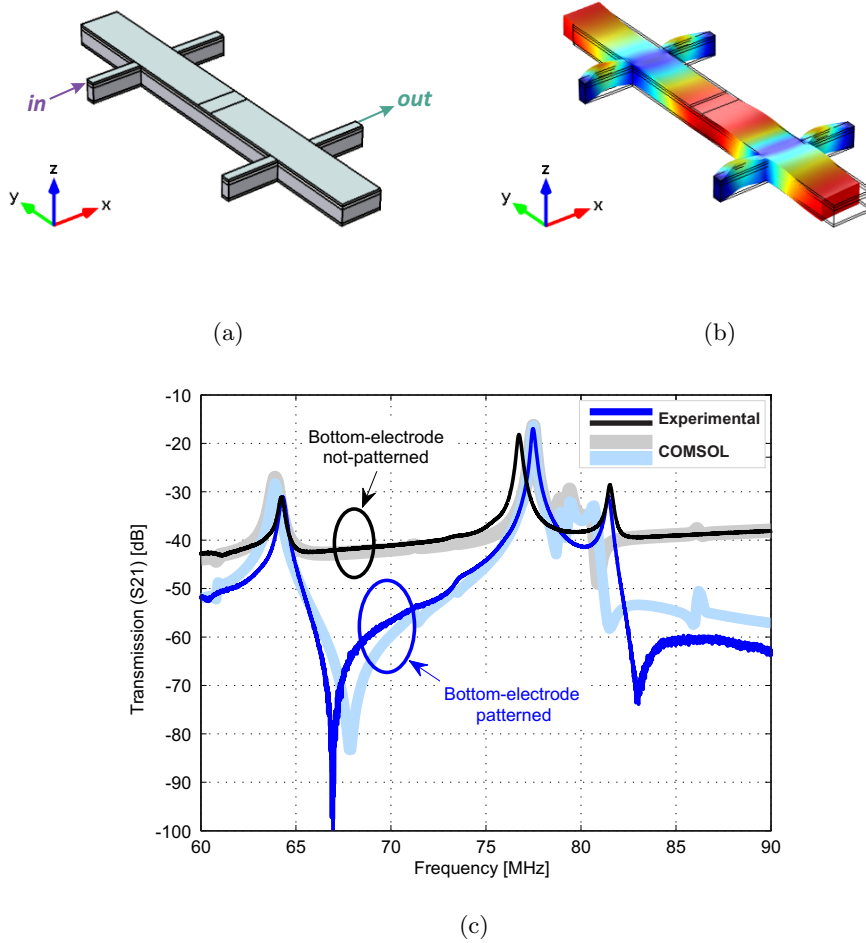


Figure 3.7: (a) A schematic of Set I resonator with one-input and one-output electrode, (b) simulated mode shape of the resonance, (c) experimental and finite element simulation transmission of the resonators with patterned and un-patterned bottom electrode, Type(a) and (b).

As seen, the absolute value of  $e_{31}$  increased from  $-1.99$  to  $-7.00$  C/m<sup>2</sup> with DC-bias voltage in the range of 0-3 V. The variation of the  $e_{31}$  with the DC-bias voltage is associated with the piezoelectric domain re-orientation process. At low DC-bias voltages (0-2 V), the main contribution to the  $e_{31}$  is due to the increase in the domain reversal with increasing DC-bias voltage. At higher DC-bias voltages (above 2 V), most switchable domains have already been aligned along the direction of the DC-bias voltage, the  $e_{31}$  variation has become saturated and is smaller since it is determined mainly by the variations of the dipoles [63].

By applying the DC-bias voltage, the motional impedance is decreasing due to the enhancing of the  $e_{31}$ . Therefore, as seen in Fig. 3.5, by applying the DC-bias voltage, the passband gain of the resonator increases. The motional-capacitance ( $C_m$ ) and -inductance ( $L_m$ ) have been extracted and reported in Table 3.2. Also by applying the DC-bias voltages, the resonator's efficiency increases, but as depicted in Table 3.2, the resonance frequency is quite constant.

Table 3.2: The patterned bottom-electrode resonator's performance at different DC-bias voltages.

Set	DC-bias [V]	$f_{res}$ [MHz]	$Q$ -factor	$C_m$ [fF]	$L_m$ [mH]	$R_m$ [ $\Omega$ ]	$e_{31}$ [C/m <sup>2</sup> ]
(I)	0	77.49	704	0.86	4.90	3390	-1.99
	1	77.48	482	3.02	1.40	1410	-3.72
	2	77.46	368	7.33	0.57	762	-5.80
	3	77.48	322	10.75	0.39	597	-7.00
(II)	0	76.46	956	0.78	5.41	2754	-1.64
	1	76.44	637	3.26	1.29	988	-3.35
	2	76.43	449	9.72	0.43	471	-5.78
	3	76.45	402	14.29	0.29	348	-7.01
(III)	0	74.69	830	1.19	3.82	2164	-1.48
	1	74.66	574	4.07	1.11	908	-2.74
	2	74.66	439	10.55	0.43	459	-4.41
	3	74.65	373	17.94	0.25	318	-5.75

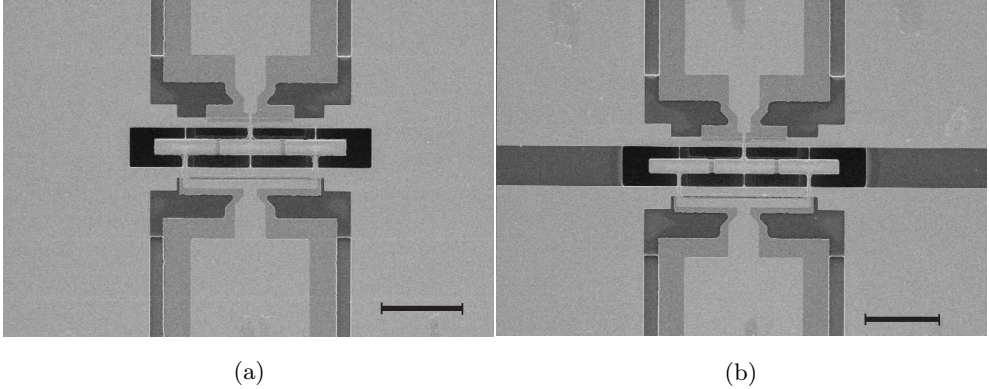
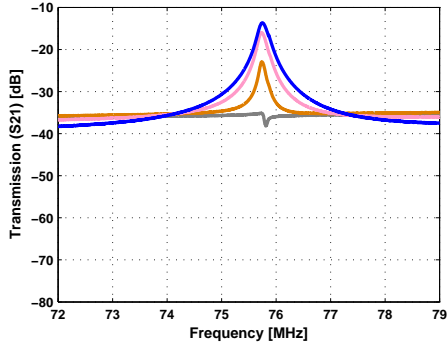


Figure 3.8: Scanning electron micrograph (SEM) of a PZT-on-silicon resonator (two-input and one-output electrodes) with (a) un-patterned ground, and (b) patterned ground, (Scale bar 50  $\mu\text{m}$ ).

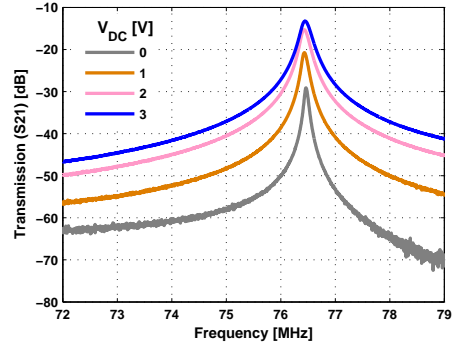
Using the extracted  $e_{31}$  coefficient at DC-bias voltage of 3 V, the finite-element simulation is performed for case studies of Type(a) and (b). For this simulation only the main resonance peak has been fitted to experimental results by varying the silicon thickness in the range of  $\pm 0.5 \mu\text{m}$  due to the silicon device layer thickness accuracy of the wafer at different spots of the wafer. As seen in Fig. 3.7(c) there is a good agreement between the experimental and simulation results. Fig. 3.7(c), shows the finite-element simulation has good agreement on the spurious modes predictions. The measured frequency responses shows some shifts in the resonance frequencies. The finite-element simulation shows that the electrode-patterning is not the cause of the resonance frequency shift and could be due to the silicon device layer thickness variation or some mechanical aspects due to the electrode patterning.

### 3.5.2 Set II: Two-Input and One-Output Electrodes (Asymmetrical Configuration)

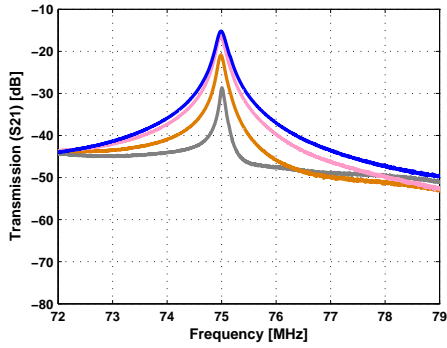
The frequency response of Set II devices (Fig. 3.8) for different DC-bias voltages are shown in Fig. 3.9. The Fig. 3.9 sequences follow as the Fig. 3.1 order. Fig. 3.1(a) shows a very small stopband response at 0 DC-bias voltage. By comparing Fig. 3.9(a) and (b), the patterning of the bottom-electrode improves the stopband rejection by more



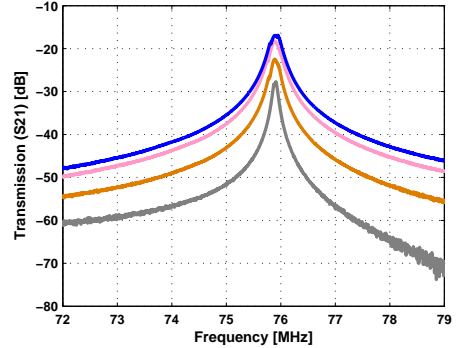
(a)



(b)



(c)



(d)

Figure 3.9: Measured transmission of Set II resonators using  $50\ \Omega$  termination with (a) un-patterned bottom-electrode and ground, (b) patterned bottom-electrode and un-patterned ground, (c) un-patterned bottom-electrode and patterned ground, (d) patterned bottom-electrode and ground.

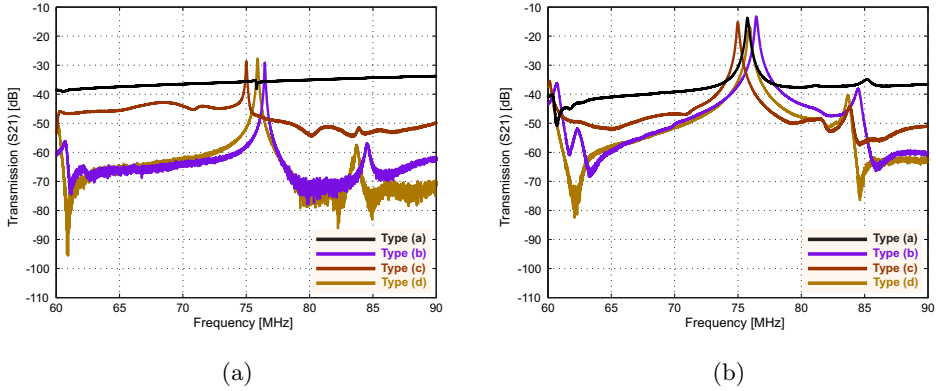


Figure 3.10: Measured frequency response of Set II resonators with four different electrode patternings (a) without DC-bias voltage and (b) DC-bias voltage of 3V

than 20 dB and 10 dB at DC-bias voltage of 0 V and 3 V, respectively. Fig. 3.9(b) and (d), show a slightly different response. As seen in Fig. 3.9(c), same as the Set I devices, patterning the ground can improve the performance. The extracted data for Type (b) of Set II devices are listed in Table 3.2. The motional impedances at all DC-bias voltages are improved compared to the Set I devices with quite close range of  $e_{31}$ . There is a slight improvement in the  $Q$ -factors. The main reason is the increasing  $\Gamma$  value from 2 for Set I to  $\frac{8}{3}$  for Set II and therefore reducing the motional impedance. As Set II devices contain  $1\frac{1}{2}$ -wavelength with the total length of 128  $\mu\text{m}$ , therefore the captured wavelength is  $\lambda_2=85.33\ \mu\text{m}$ . This wavelength is bigger than the wavelength of Set I devices with the wavelength (total length) of  $\lambda_1=84\ \mu\text{m}$ . Therefore as seen, the resonance frequencies of Set II devices are lower than the Set I devices. This is due to the one extra spacing at Set II devices compared to the Set I devices. Wider frequency range of Set II devices are presented in Fig. 3.10. As seen, the resonators responses are similar to the Set I. devices, Fig. 3.6. The effect of the bottom-electrode and ground patternings are clearly depicted in Fig. 3.9, which follows the Set I responses, Fig. 3.6.

The finite-element simulation results are presented in Fig. 3.11. As seen, by matching the main resonance peak position of the resonators by varying the silicon thickness, the simulation can predict the resonance path and the main spurious modes very well. In this simulation the grounding resistances at input and output sides have been set

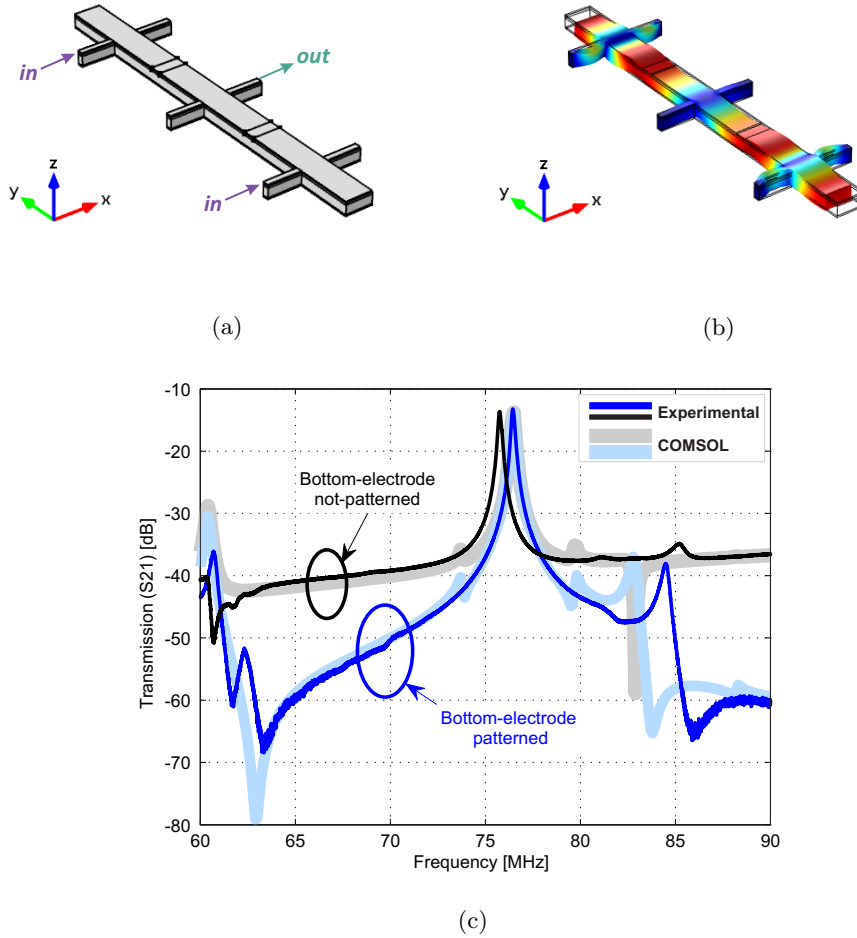


Figure 3.11: (a) A schematic of Set II resonator with one-input and one-output electrode, (b) simulated mode shape of the resonance, (c) experimental and finite element simulation transmission of the resonators with patterned and un-patterned bottom electrode, Type (a) and (b).

differently (input grounding resistance is half of the output one) as they are asymmetrical as well. It should be mentioned that the chosen damping (and therefore the  $Q$ -factor) is constant at all the simulated frequencies which is in reality is different and each spurious mode has a different  $Q$ -factor and maybe this is the reason to see a difference between the strength of the simulated spurious modes and the measured results. As seen in this simulation, the middle anchor is quite straight compared to the side anchors. This is due to not having the overhanging area [50] (half of the spacing) in the devices. Maybe by adding an optimum overhang area [73] the  $Q$ -factor of the devices may increase. This issue has been seen in the Set I simulation as well, Fig. 3.11(b).

### 3.5.3 Set III: Three-Input and Two-Output Electrodes (Asymmetrical Configuration)

This set of the devices contains three-input and two-output electrodes with four spacing in between. Set III devices (Fig. 3.12) have total length of  $216\ \mu\text{m}$  which captures  $2\frac{1}{2}$ -wavelength with the wavelength of  $\lambda_3 = 86.4\ \mu\text{m}$ . As  $\lambda_3 > \lambda_2 > \lambda_1$ , therefore as shown in Fig. 3.13, the resonance frequencies of Set III devices are lower than both Set II and Set I resonance frequencies. Set I, Set II and Set III have one, two and four spacings, respectively. Therefore, by comparing the resonator responses it is clear that the resonance frequency difference between Set III and Set II are more than the difference between Set II and Set I resonance frequencies which is due to the number of spacing difference between the sets.

Fig. 3.13(a), shows decreasing the insertion loss with invariant rejection floor with increasing DC-bias. The frequency response is improving by patterning the bottom-electrode and the ground, Fig. 3.13(b), (c) and (d). As seen in Fig. 3.13(b) and (d), the responses are similar. Comparing the response of Fig. 3.13(a) and (c), by patterning the ground the rejection floor is improved around 10 dB. The frequency response trends due to the patternings are similar to the previous sets. The extracted data for Type(b) of Set III devices are listed in Table 3.2. As seen, these devices show lower  $e_{31}$  coefficient compared with Set I and Set II devices. The motional impedances are improved. This set shows better  $Q$ -factor than Set I and lower than Set II devices. The wider frequency range of the responses are presented in Fig. 3.14. The finite-element simulation results of Type(a) and (b) of Set III devices are presented in Fig. 3.15. As seen, the simulation can predict the behavior very good including the position of

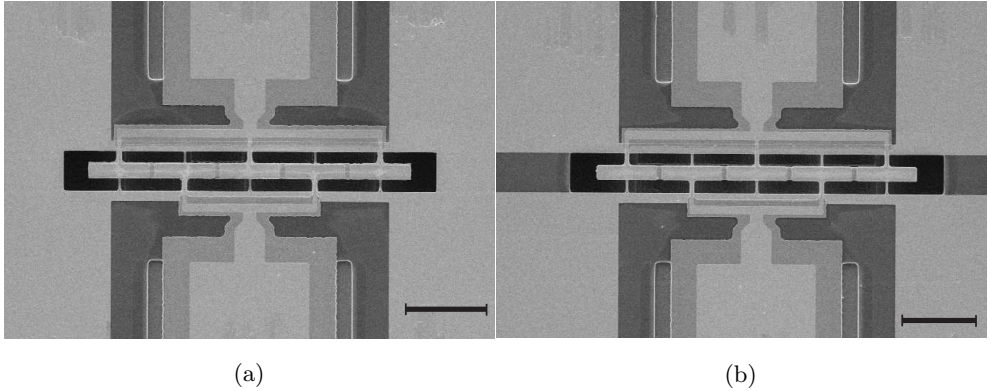


Figure 3.12: Scanning electron micrograph (SEM) of a PZT-on-silicon resonator (three-input and two-output electrodes) with (a) un-patterned ground, and (b) patterned ground, (Scale bar 50  $\mu\text{m}$ ).

spurious modes. Regarding to the anchors, the middle anchor stands straight and anchors in the end -sides are deflecting most due to the overhanging issue which is described previously. This issue can be solved in future designs by considering the overhanging area which can improve the  $Q$ -factor.

## 3.6 Conclusions

In this chapter three sets of devices of higher-order mode resonators with PZT-on-Silicon transduction method were presented. The three sets are with 1-,  $1\frac{1}{2}$ - and  $2\frac{1}{2}$ -wavelength around 75 MHz. Each set contains devices with and without bottom-electrode and ground patternings which in total twelve different devices were characterized. The resonators shows low insertion loss using  $50\ \Omega$  termination. The ground patterning concept was presented for the first time which shows quite considerable effect on increasing the rejection floor with respect to the un-patterned bottom-electrode devices. This gives an opportunity when the patterning of bottom-electrode is not possible due to fabrication limitations. The effect of bottom-electrode and ground patterning are showing a coherent behavior on all the sets. A 3D fully-coupled (electro-mechanical) finite-element simulation is presented for the bottom-electrode pattern-

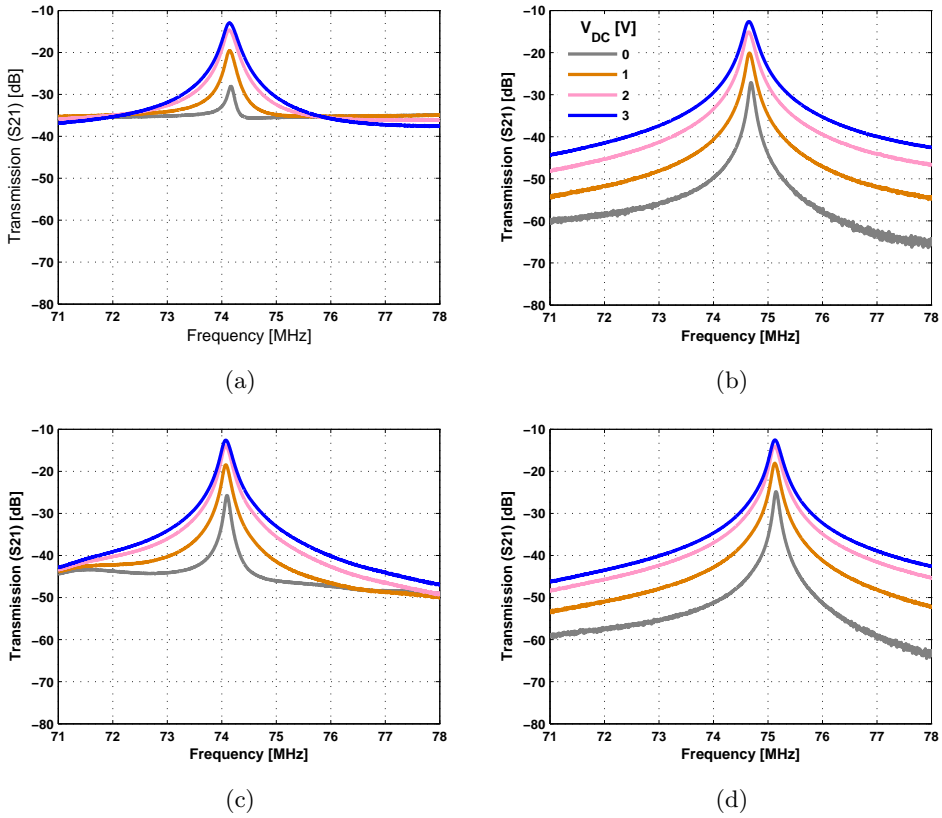


Figure 3.13: Measured transmission of Set III resonators using  $50\ \Omega$  termination with (a) un-patterned bottom-electrode and ground, (b) patterned bottom-electrode and un-patterned ground, (c) un-patterned bottom-electrode and patterned ground, (d) patterned bottom-electrode and ground.

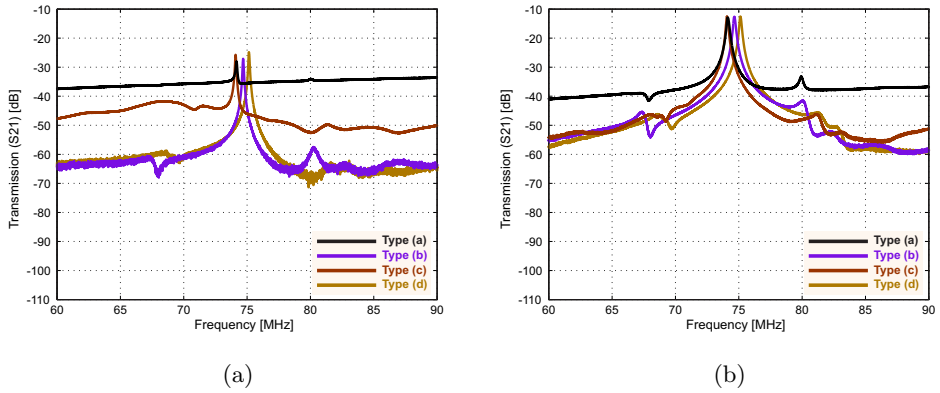


Figure 3.14: Measured frequency response of Set III resonators with four different electrode patternings (a) without DC-bias voltage and (b) DC-bias voltage of 3V

ing cases of all the sets. Finite-element simulation shows a good agreement with the measurement results including an acceptable prediction for the spurious modes. The finite-element simulation approach can be used for future designs.

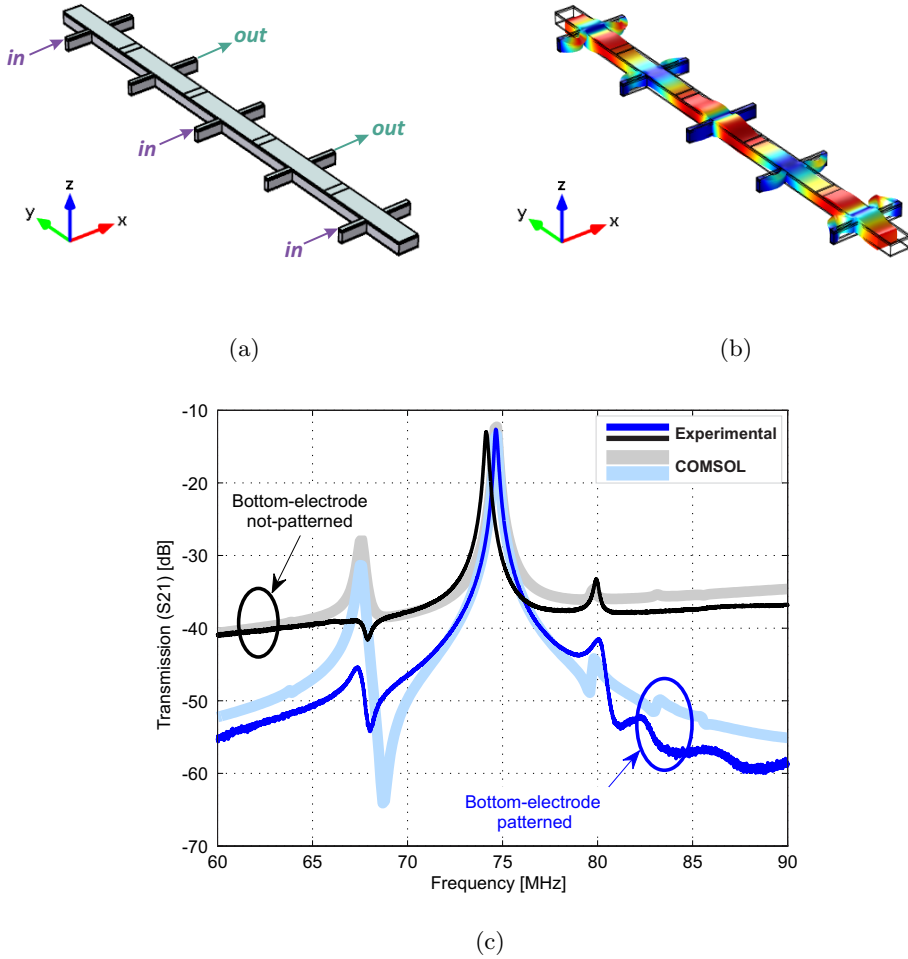


Figure 3.15: (a) A schematic of Set I resonator with one-input and one-output electrode, (b) simulated mode shape of the resonance, (c) experimental and finite element simulation transmission of the resonators with patterned and un-patterned bottom electrode, Type (a) and (b).

## Chapter 4

# A Mechanically Coupled Contour Mode Bandpass Filter

In this chapter, a bandpass filter using two mechanically coupled contour mode resonators is presented. The filter is presented at a resonance frequency of around 380 MHz. The filter consists of two mechanically-coupled resonators with the same designed wave-length. The filter is fabricated using 500 nm-thick pulsed-laser deposited (PLD) lead zirconate titanate (PZT) on top of 3  $\mu\text{m}$  silicon (PZT-on-Silicon). The bottom-electrode-patterning technique has been applied for the resonators. The filter is characterized using a four-port measurement with  $50\ \Omega$  termination. Using this technique, the filter insertion loss improved around 6 dB as well as the notches of the filter.

### 4.1 Introduction

Mechanically- and/or electrically-coupling methods are most common ways for coupling several single resonators to get a bandpass filter performance. For Lamb-wave RF-MEMS filters, these techniques are still under development and so far several methods have been presented [52, 51, 50, 64]. In this work, differentially actuated and read-out methods have been used for two mechanically coupled resonators. A

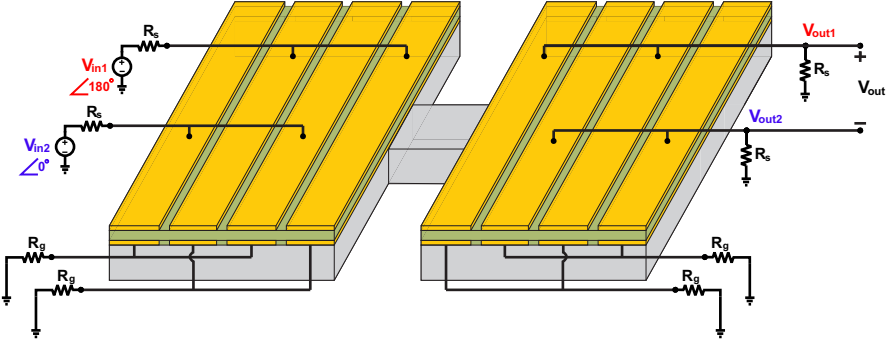


Figure 4.1: A schematic of a mechanically coupled contour-mode resonators with differentially actuation and readout.

schematic of the resonators are shown in Fig. 4.1. As seen, there are two input signal with  $180^\circ$  phase difference. To obtain the highest performance, this phase difference is needed for the actuation due to the waveform and the electrodes locations. Both output signals of each resonator are terminated separately and the output signal is obtained using the subtraction technique. The equivalent circuit of the filter is shown in Fig. 4.2.

All the parameters of both resonators are designed to be same. Therefore the equivalent circuit parameters ( $R_m$ ,  $L_m$  and  $C_m$ ) are the same in the model. The resonators are coupled with a mechanical coupler which is presented as a coupling capacitance ( $C_c$ ) in the equivalent circuit [52]. The length and width of the coupler will determine the loading-mass and -spring of the coupler in the equivalent circuit [51]. By choosing the length of the coupler to be equal to the quarter wavelength of the resonators will minimize the loading mass of the coupler. The width of the coupler then will define the stiffness of the coupling spring. Therefore the band width of the filter can be tuned by the coupler width.

## 4.2 Fabrication And Characterization

Fabrication of the devices are mainly based on the process presented in the previous chapters. Each resonator consists of a 500 nm pulsed-laser deposited (PLD) lead zirconate titanate (PZT) thin-film on top of a  $3\ \mu\text{m}$  silicon (PZT-on-Si). The PZT and

Pt layers are etched on top the coupler. The coupler size is determined in the dry etching step. By boosting the resonance frequencies of the resonators, the quarter wavelength as an optimal (easiest) designing approach for the coupler. However, at high frequencies, this is a big fabrication challenge. Therefore, the size of the coupler in this work is bigger than the quarter wavelength of the resonators. Therefore, the coupler here will have a mass-loading effect on the resonances.

The SEM image of the fabricated device is presented in Fig. 4.3. As seen, port 1 and port 2 are two input electrodes and port 3 and port 4 are the outputs. The size of each resonator is  $30 \times 80 \mu\text{m}^2$ . The coupler size is  $14 \times 21 \mu\text{m}^2$ . To cancel the feed-through signal of each resonator, the bottom-electrode patterning method has been utilized for both resonators [74, 60]. The device is characterized in an RF probe station using GSGSG probes and a 4-port Agilent N5244A network analyzer. A 4-port SOLT calibration has been performed using Agilent Electronic Calibration Module up to the probes. All the measurements have been done by applying 0 dBm input power.

The measured transmission of the filter is shown in Fig. 4.4 from 200 MHz up to 1 GHz using 4 V DC-bias voltage. The designed resonance frequency of the filter is highlighted. As seen, the filter shows a dominant designed peak in a long frequency range. The rejection floor is around  $-27$  dB and the insertion loss is about  $-16$  dB. The short range of the filter response and its phase change are presented in Fig. 4.5(a) and (b). The filter contains two notches at both side of the filter response. For com-

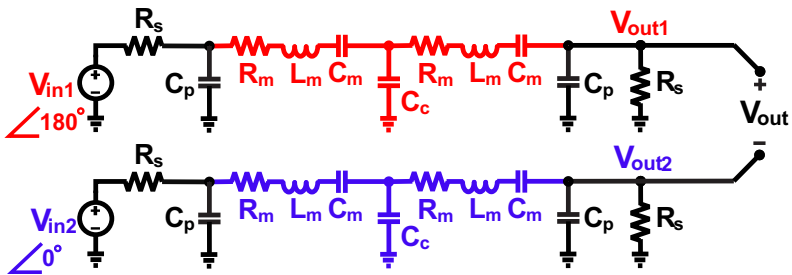


Figure 4.2: Equivalent circuit of the filter with differential readout and actuated resonators.

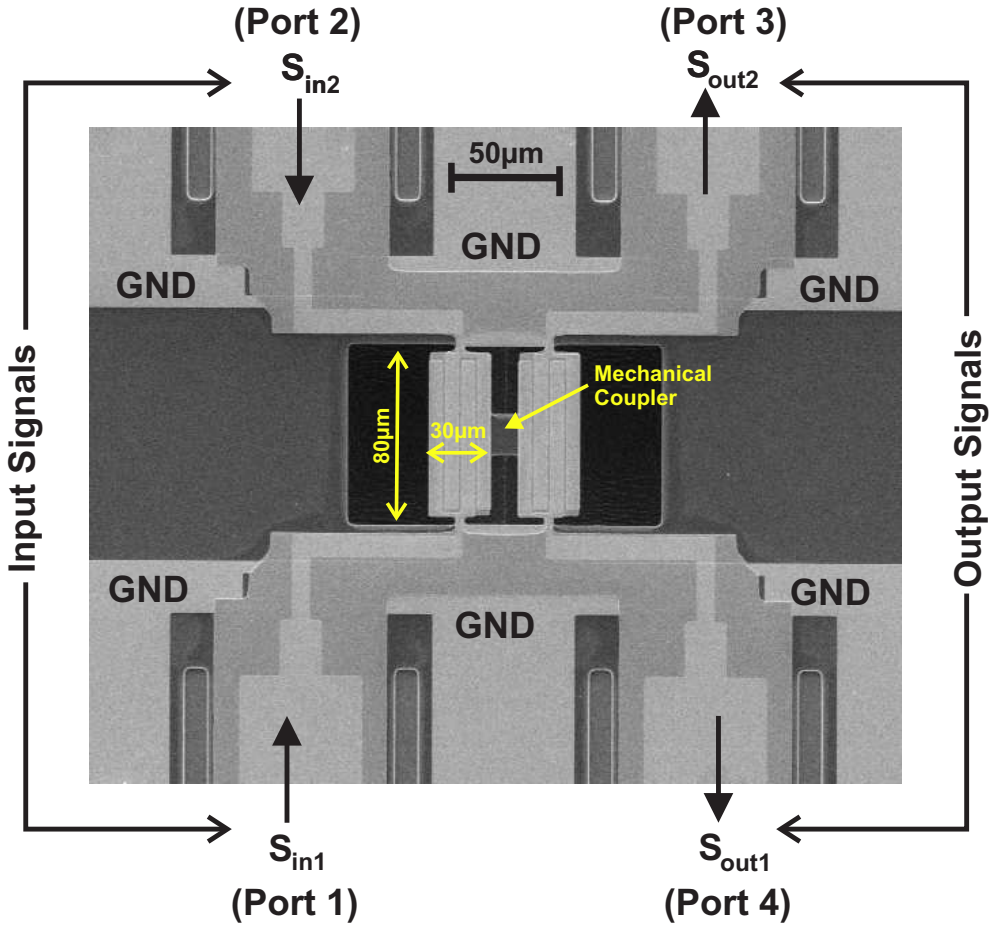


Figure 4.3: Scanning electron micrograph (SEM) of a mechanically coupled PZT-on-silicon filter at 380 MHz.

parison, the transmission of each path ( $S_{31}$  and  $S_{42}$ ) while the loaded other terminals are presented in Fig. 4.6 on top of the differential filter response ( $S_{dc21}$ ). The differential filter response shows 6 dB improvement compared to each path filter. The notch in both sides of the resonance peak shows a considerable improvement as well. Using this technique, the rejection floor of the differential filter does not change. The reason for this is both paths are actuated with  $180^\circ$  phase difference and the feed-through signals have the same phase difference. By subtracting the output signals of the paths, the feed-throughs of each path are added and therefore the rejection stays the same.

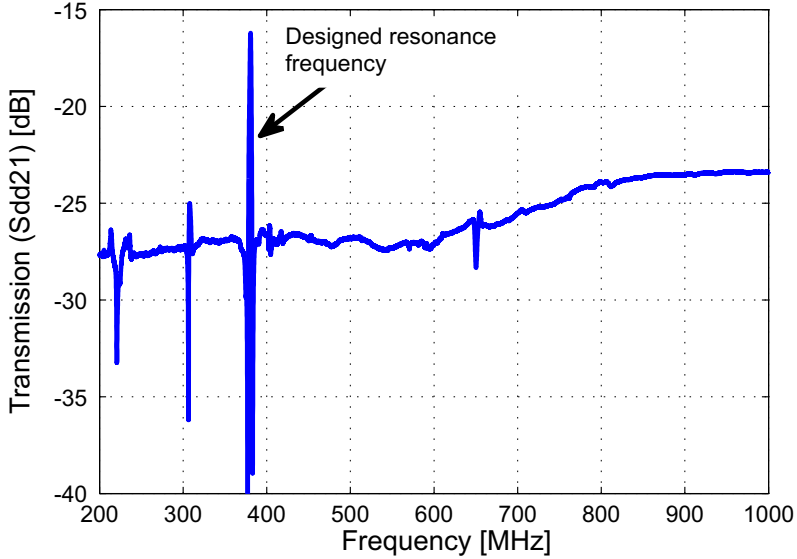


Figure 4.4: Measured transmission of the filter from 200 MHz up to 1 GHz with  $50\ \Omega$  termination.

The measured filter response at different DC-bias voltages 0-4 V with 1 V increments is presented in Fig. 4.7. In Fig. 4.6, the single path responses are presented while the other terminals were loaded. The response of the single paths while the other terminals are open is presented in Fig. 4.8. As seen the two-pole response of the filter is more visible.

### 4.3 Conclusion

In conclusion, the differentially actuated and readout method is an approach to be able to improve the filter insertion loss by around 6 dB as well as the notch of the filter. The rejection floor of the filter is not getting improved compared to the single path filters.

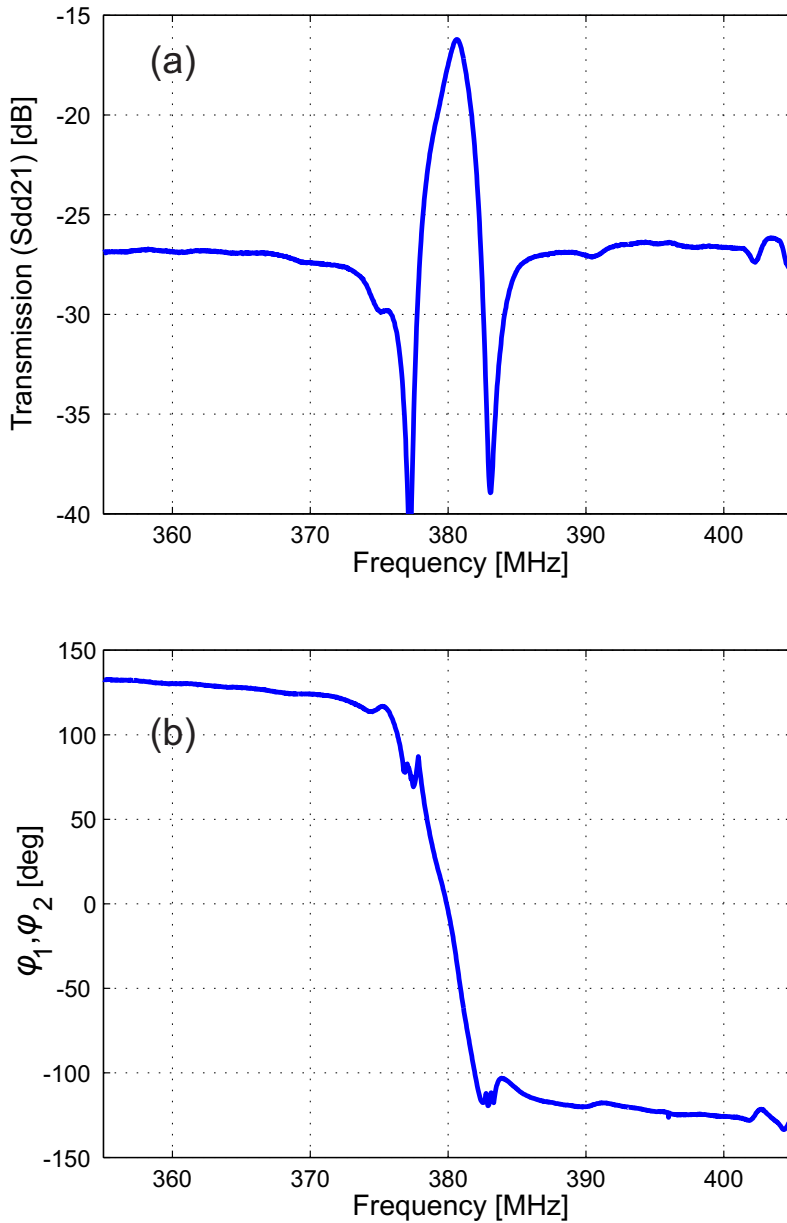


Figure 4.5: (a) Measured transmission of the filter, (b) The measured phase change of the resonators.

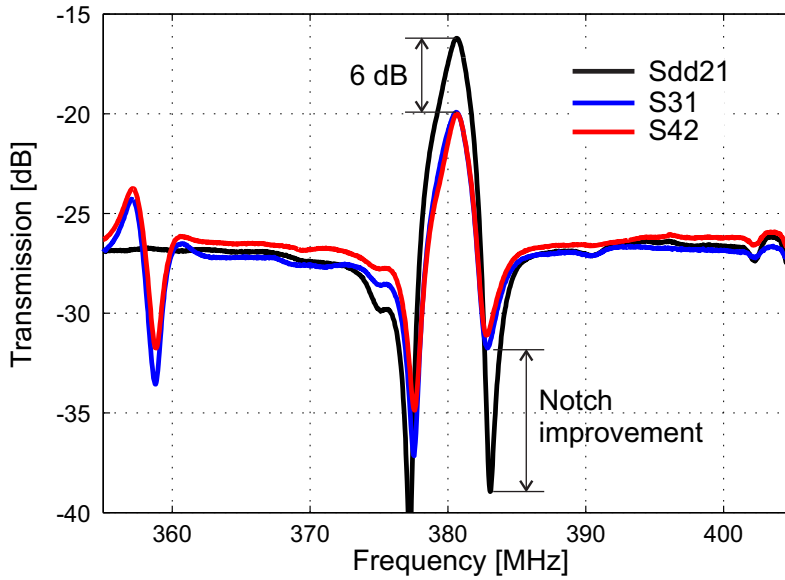


Figure 4.6: Measured transmissions of the single path filters ( $S_{31}$  and  $S_{42}$ ) with other ports terminated and the differential filter  $S_{dd21}$ .

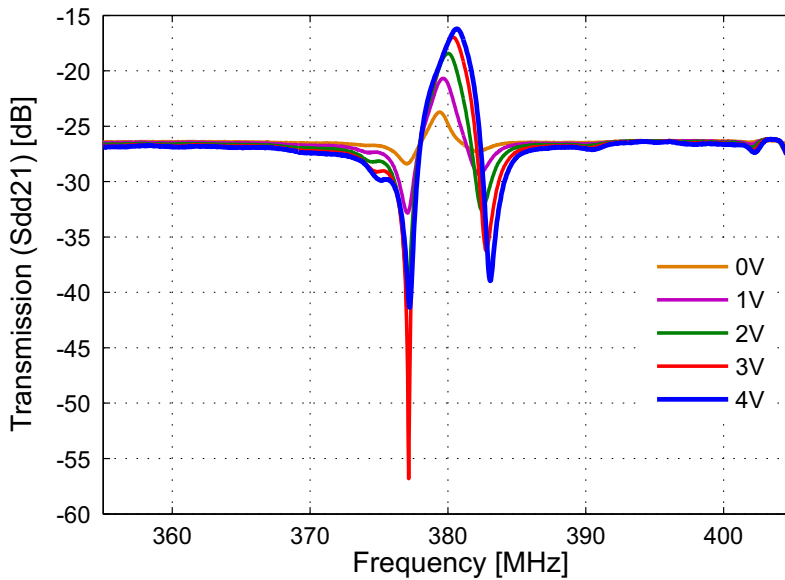


Figure 4.7: Measured transmission of the filter at different DC-bias voltages from 0-4 V with 1 V increments.

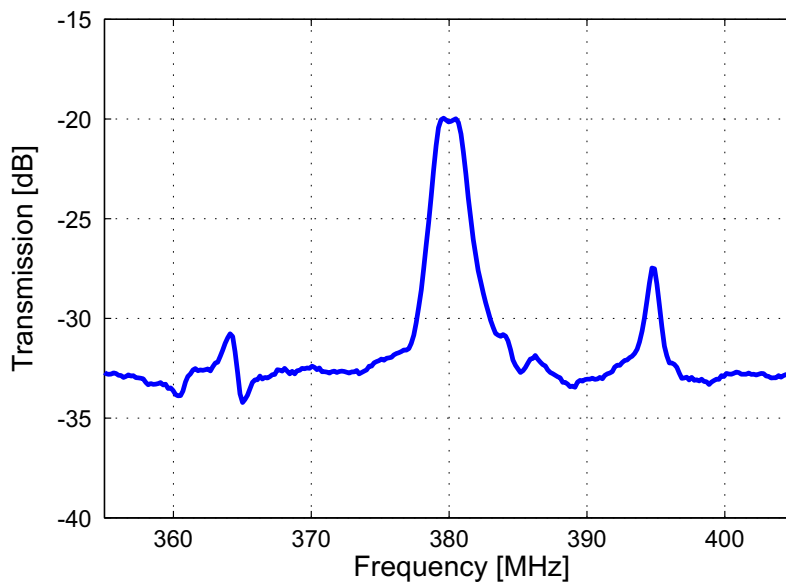


Figure 4.8: Measured transmission the single path filter with other unloaded terminals.

## Chapter 5

# A 4th-Order Bandpass Filter Based on Differential Readout<sup>1</sup>

A new 4th-order band-pass filter (BPF) method based on the subtraction of two 2nd-order contour-mode Lamb-wave resonators is presented. Two case studies have been presented at around 380 MHz and 700 MHz. Each case study consists of two resonators which have slightly different resonance frequencies around 380 MHz and 700 MHz. Each resonator consists of a 500 nm pulsed-laser deposited (PLD) lead zirconate titanate (PZT) thin-film on top of a 3  $\mu\text{m}$  silicon (PZT-on-Si). The resonators are actuated in-phase and their outputs are subtracted. Utilizing this technique, the feed-through signals are eliminated, while the outputs of the resonators are added up constructively, due to the phase difference between the two output signals. The BPF is presented using 50  $\Omega$  termination. This technique provides further opportunities for MEMS filter design in addition to existing methods, i.e. mechanical and/or electrical coupling. It also resolves the design issue associated with high feed-through, when

---

<sup>1</sup>This chapter has been published in:

H. Yagubizade *et al.*, "A 4th-order band-pass filter using differential readout of two in-phase actuated contour-mode resonators," *Appl. Phys. Lett.* **103** 173517, 2013.

and accepted in

H. Yagubizade *et al.*, "A UHF 4th-order bandpass filter based on contour-mode PZT-on-Silicon resonators," *IEEE Micro Electro Mechanical Systems, (MEMS)*, 2014.

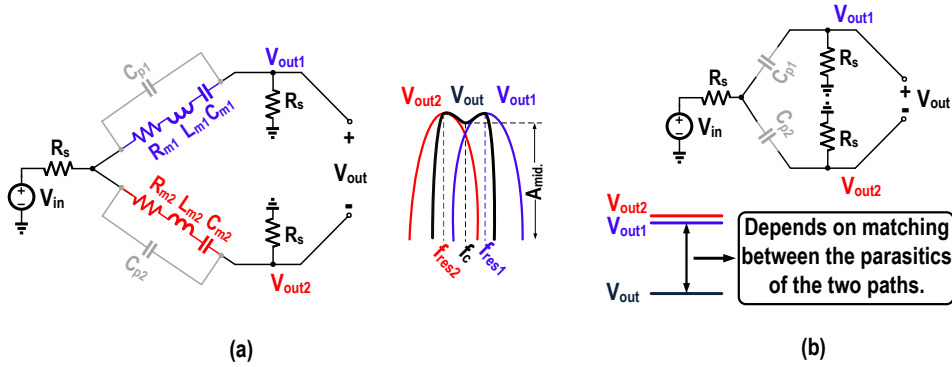


Figure 5.1: (a) Equivalent circuit of 4th-order filter with differential readout of two in-phase actuated resonators, including the motional capacitances,  $C_{m1}$ ,  $C_{m2}$ , inductances,  $L_{m1}$ ,  $L_{m2}$ , impedances,  $R_{m1}$ ,  $R_{m2}$ , feed-through capacitances,  $C_{p1}$ ,  $C_{p2}$ , and termination impedance,  $R_s$ . (b) Simplified model of the resonators for frequencies outside the passband of the resonator.

exploiting piezoelectric materials with high-dielectric constant like PZT.

## 5.1 Introduction

RF-MEMS filters are providing new opportunities for the next generation of wireless communication systems enabling low power consumption and high level of integration. FBAR [12] is most successful among available RF-MEMS filters and is already commercialized. The current demand requires the integrability of filters at different resonance frequencies compacted in the same die fabricated in a single process. The center frequency of FBAR resonators is determined by the thickness of the piezoelectric layer [12, 75]. As a consequence, realizing FBAR resonators in the same substrate with different resonance frequencies is a difficult task. Lamb-wave MEMS resonators, where resonance frequency is set by lateral dimensions rather than the vertical dimension, have been proposed to overcome this issue [47, 14]. Lamb-wave resonators are released from the substrate and therefore have a higher quality factor, which is crucial in synthesizing narrow-band channel select filters required in RF front-ends [64, 69, 52]. Lamb-wave filters are still in the research stage and differ-

ent filter configurations, such as mechanically- and/or electrically-coupling [51, 64] methods, are under development.

AlN [12, 69, 64], ZnO [54, 14], lithium niobate [76, 77] and recently PZT [74, 58, 60, 61, 53] thin-films are the prevalent piezoelectric materials utilized in Lamb-wave resonators. Of these, PZT has the highest electromechanical coupling-factor [47]. Because of this, devices with PZT can be made several times smaller without incurring extra insertion losses. The main advantage is the reduction in area consumed by the resonator for the same motional impedance, which is a key factor in lowering the cost and form-factor of wireless devices. On the other hand, PZT suffers from high feed-through (i.e. higher parasitic capacitance), due to its high dielectric permittivity and, as a consequence, drastically reduces the stopband rejection [74, 60, 61]. This fact limits the applicability of PZT application for high frequencies. Recently, a method was presented to cancel the feed-through signal in 2-port PZT-based single resonators below 100 MHz [74]. The presented method has improved the stopband rejection by more than 20 dB utilizing a bottom-electrode patterning technique. Nevertheless, to widen the applicability of PZT-based resonators to higher frequencies further mitigation of the undesired feed-through signals is imperative.

In this chapter, we propose an RF-MEMS filter design approach, which is not based on the traditional methods such as mechanical and/or electrical couplings. Simultaneously, this method is effective for improving the stopband rejection by canceling the feed-through signal, which is more crucial in high-dielectric materials such as PZT especially at frequencies above 100 MHz.

## 5.2 Concept And Simulation

The idea is conceptually presented in Fig. 5.1. The resonators are actuated independently in-phase and the output of the resonators are subtracted. The resonance frequency of resonators 1 and 2 ( $f_{\text{res1}}$  and  $f_{\text{res2}}$ ) are slightly different. At the center frequency ( $f_c$ ) in between  $f_{\text{res1}}$  and  $f_{\text{res2}}$ , the output phase of the resonators ( $\varphi_1$  and  $\varphi_2$ ) are approximately  $\varphi_1 = -\varphi_2$  and for frequencies outside the passband of the filter,  $\varphi_1$  and  $\varphi_2$  are approximately equal ( $\varphi_1 = \varphi_2$ ). Therefore, for frequencies in between  $f_{\text{res1}}$  and  $f_{\text{res2}}$ , the signals will add up and outside this frequency range they will cancel. This concept has two interesting implications. Firstly, it generates a 4th-order filter out of uncoupled 2nd-order resonators and secondly, the feed-through signal throughout the frequency range will be canceled. The transfer function of each

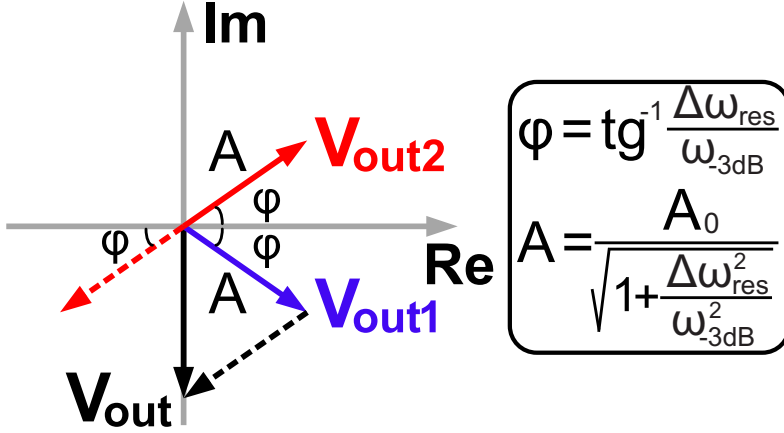


Figure 5.2: Complex plane representation of two in-phase actuated resonators and subtracted outcome at center frequency ( $f_c$ ).

resonator can be expressed as

$$H_i(s) = \frac{V_{\text{out},i}}{V_{\text{in}}} = \frac{R_s}{L_{m,i}} \times \frac{s}{s^2 + \omega_{-3\text{dB},i} \times s + \omega_{\text{res},i}^2}, i = 1, 2 \quad (5.1)$$

where  $\omega_{-3\text{dB},i}$  and  $\omega_{\text{res},i}$  are respectively the bandwidth  $(2R_s + R_{m,i})/L_{m,i}$  and the resonance frequency  $1/\sqrt{L_{m,i}C_{m,i}}$  of the  $i$ th path.  $L_m$  can be derived for contour-mode resonators as

$$L_m = \frac{1}{4N} \times \frac{D \times t_{\text{tot}} \times \rho_{\text{eff}}}{w_e} \times \frac{1}{e_{31}^2}. \quad (5.2)$$

where  $N$  is the number of fingers on the input-/output-port.  $D$  is the depth of the resonator and  $t_{\text{tot}}$  the resonator total thickness.  $\rho_{\text{eff}}$  is the effective density and  $w_e$  is the electrode width.

Assuming  $L_{m,1} = L_{m,2} = L_m$  and  $R_{m,1} = R_{m,2} = R_m$ , the total transfer function of the filter after subtraction can be expressed as

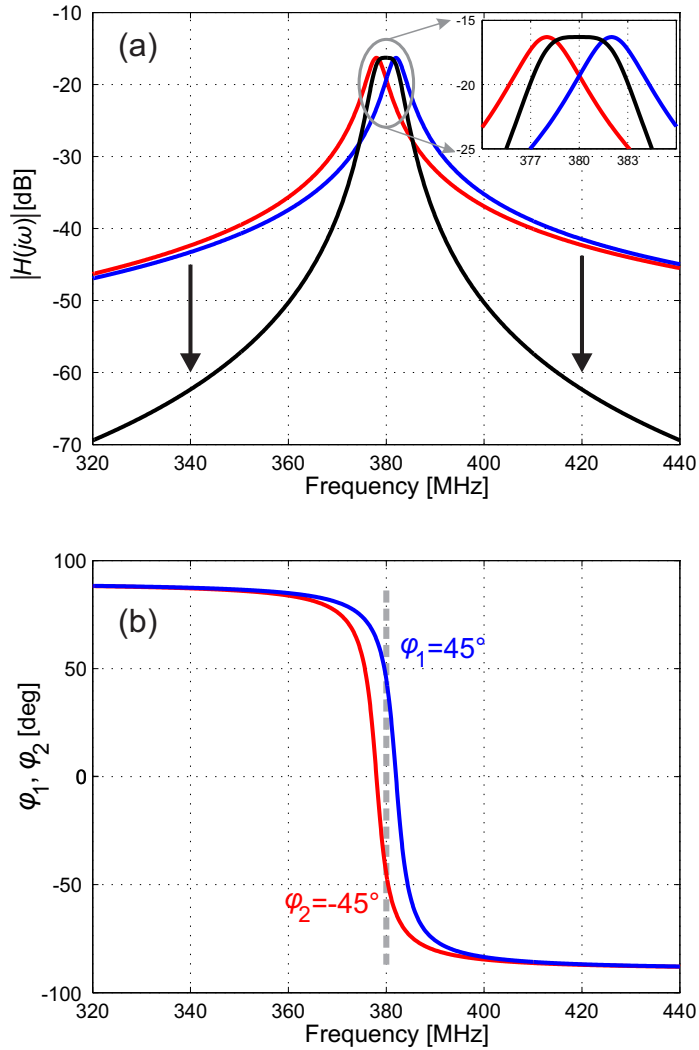


Figure 5.3: (a) The simulation results of a 4th-order filter using subtracting of two 2nd-order resonators with slightly different resonances with  $\omega_{-3dB, i} = \Delta\omega_{res}$  and (b) the phase change of the resonators and illustration of the fact that  $\varphi_1 = -\varphi_2$  at the center frequency of the filter.

$$\begin{aligned}
 H(s) &= \frac{V_{\text{out1}} - V_{\text{out2}}}{V_{\text{in}}} \\
 &= \frac{R_s}{L_m} \times \frac{2\omega_c \times \Delta\omega_{\text{res}} \times s}{(s^2 + \omega_{\text{-3dB}} \times s + \omega_{\text{res},1}^2) \times (s^2 + \omega_{\text{-3dB}} \times s + \omega_{\text{res},2}^2)}
 \end{aligned} \tag{5.3}$$

where  $\omega_c = (\omega_{\text{res},1} + \omega_{\text{res},2})/2$ . Assuming  $A_0 = R_s/(2R_s + R_m)$  and  $\omega = \omega_c + \delta\omega$ , allows Eq. 5.1 to be simplified for  $\delta\omega \ll \omega_c$ , resulting in

$$H_i(j\omega) \cong \frac{A_0}{1 + \frac{j}{\omega_{\text{-3dB}}/2} \times (\delta\omega \pm \Delta\omega_{\text{res}}/2)}, i = 1, 2 \tag{5.4}$$

Using Eq. 5.4, the amplitude and the phase of the total output of the filter at  $\omega_c$  are shown in Fig. 5.2. As seen, by increasing  $\Delta\omega_{\text{res}}$ ,  $\varphi$  increases and the output vectors of each resonator are adding up more constructively. However, at the same time, the magnitude of each resonator decreases. Therefore, there must be an optimum  $\Delta\omega_{\text{res}}$  to maximize the total output of the filter at  $\omega_c$  ( $A_{\text{mid.}}$ ) and hence reducing the ripple of the filter. It can be shown that the optimum  $\Delta\omega_{\text{res}}$  equal the bandwidth of each resonator ( $\Delta\omega_{\text{res}} = \omega_{\text{-3dB},i}$ ), which leads to an optimum value of  $A_{\text{mid.}} = A_0$  and  $\Delta\varphi = \pi/4$ . If  $\Delta\omega_{\text{res}} > \omega_{\text{-3dB},i}$ , the filter response will contain a certain ripple which increases with increasing  $\Delta\omega_{\text{res}}$ . If  $\Delta\omega_{\text{res}} < \omega_{\text{-3dB},i}$ , the filter response will have zero ripple but the insertion loss of the filter will increase.

Taking for calculation a filter with a center frequency of  $f_c = 380$  MHz, two resonators at resonance frequencies of  $f_{\text{res1}} = 378$  MHz and  $f_{\text{res2}} = 382$  MHz and bandwidth of 4 MHz, where  $L_m$  of the resonators are designed to be around 13  $\mu\text{H}$ . The resulting transfer function of the individual resonators and the output of the 4th-order filter are presented in Fig. 5.3. As seen,  $\omega_{\text{-3dB},i} = \Delta\omega_{\text{res}}$  leads to an optimum condition of  $A_{\text{mid.}} = A_0$  (zero ripple) and  $\Delta\varphi = \pi/2$  ( $\varphi_i = \pm\pi/4$ ). On the other hand, outside the passband, the amplitude and the phase of the two paths will get closer and therefore by subtraction of their outputs, the rejection floor will improve considerably. Nonetheless, in practice, the rejection floor is limited by inherent mismatches (due to fabrication) between the parasitic feed-throughs of the individual resonators. This is illustrated in Fig. 5.1(b).

The proposed technique is realized using two contour-mode resonators, shown in Fig. 5.4(a), with slightly different resonance frequencies approximately at 380 MHz.

To cancel the feed-through signal of each resonator, the bottom-electrode patterning method [74] has been utilized for both resonators. Each resonator consists of 4 fingers with 2 fingers for the input- and output-port. The wavelength of each resonator is around  $16\ \mu\text{m}$  with around  $200\ \text{nm}$  variation between the wavelength of the resonators to provide for the slight resonance frequency difference between the resonators. Each finger has around  $8\ \mu\text{m}$  width with  $2\ \mu\text{m}$  spacing in between. The resonators consist of a composite stack of (bottom to top)  $\text{SiO}_2/\text{Si}/\text{SiO}_2/\text{Ti-Pt}/\text{PZT}/\text{Pt}$ . The fabrication process is similar to the earlier presented work by Yagubizade *et al.* [74] A  $500\ \text{nm}$  PLD-based PZT thin-film is utilized on top of an around  $3\ \mu\text{m}$  silicon layer using a highly resistive silicon-on-insulator (SOI) wafer with  $0.5\ \mu\text{m}$  buried oxide (BOX) layer.

### 5.3 Characterization

The resonators were characterized in an RF probe station using GSGSG probes and a 4-port Agilent N5244A network analyzer. A 4-port SOLT calibration has been performed using Agilent Electronic Calibration Module up to the probes. All the measurements have been done by applying  $0\ \text{dBm}$  input power. The frequency response of each fabricated resonator ( $S_{21}$  and  $S_{43}$ ) and the differential readout of the filter ( $S_{\text{dc}21}$ ) at DC-bias voltage of  $4\ \text{V}$  are shown in Fig. 5.5(a). The phase change of each resonator is presented in Fig. 5.5(b). The phase of the resonators at  $f_c$  are  $\varphi_1 = 62.84^\circ$  and  $\varphi_2 = -59.16^\circ$ . As can be seen, the resonance frequency of the resonators are at  $f_{\text{res}1} = 382.9$  and  $f_{\text{res}2} = 379\ \text{MHz}$  with  $\omega_{-3\text{dB},1} \approx \omega_{-3\text{dB},2} \approx 1.8\ \text{MHz}$ . The transmission of the filter ( $S_{\text{dc}21}$ ) at different DC-bias voltages,  $0\text{-}4\ \text{V}$ , with  $1\ \text{V}$  increments are presented in Fig. 5.6. The motional impedance of the resonators at different DC-bias voltages, considering the grounding resistance ( $R_g$ ) as well as static capacitance ( $C_0$ ), has been extracted using Eq. 5.2, assuming that  $R_m \gg R_s$ .

$$S_{21}[\text{dB}] = -20 \log \left( 1 + (R_g + R_s)^2 C_0^2 \omega_0^2 \right) - 20 \log \left( 1 + \frac{R_g}{R_s} \right) - 20 \log \left( 1 + \frac{R_m}{2R_s} \right) \quad (5.5)$$

On the other hand, using the mechanical properties of a piezoelectric-transduced resonator, the motional impedance of contour-mode resonators can be calculated as

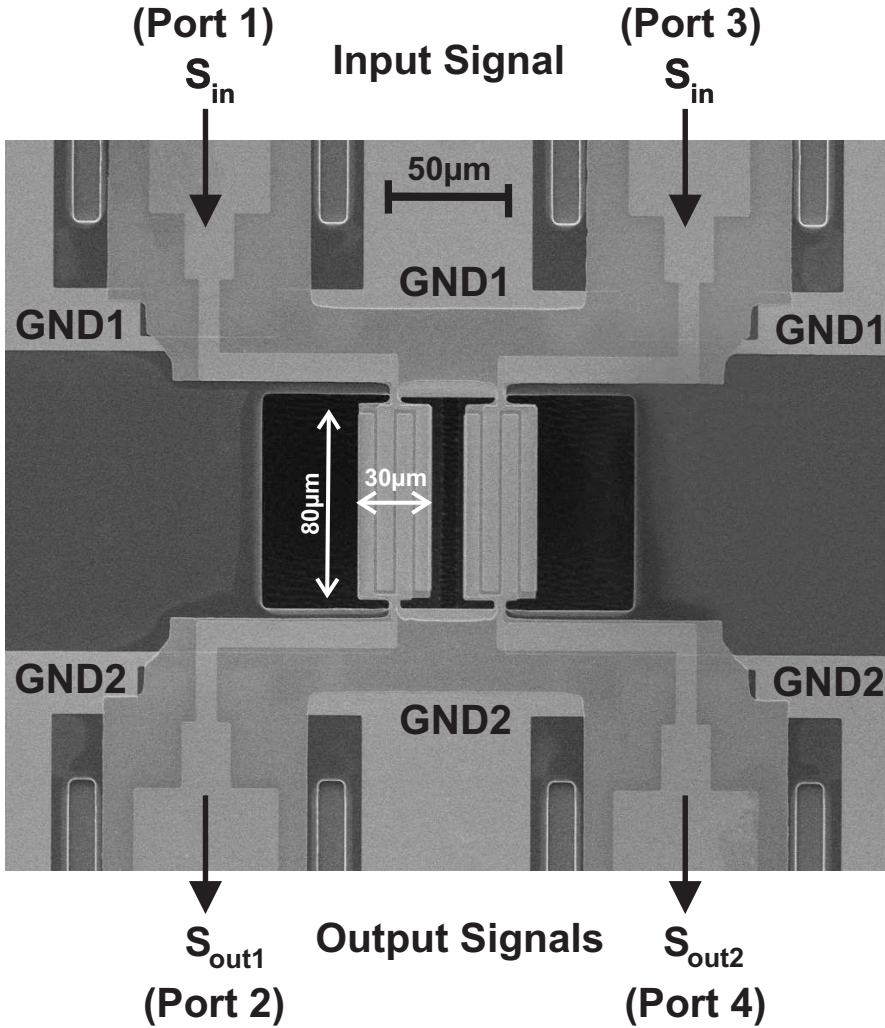


Figure 5.4: Scanning electron micrograph (SEM) of a 4th-order differential readout of in-phase actuated contour-mode PZT-on-silicon filter at 380 MHz.

$$R_m = \frac{\pi}{4N} \times \frac{\rho_{\text{eff}}^{0.5} \times E_{\text{eff}}^{0.5}}{Q} \times \frac{t_{\text{tot}}}{w_e} \times \frac{1}{e_{31}^2}. \quad (5.6)$$

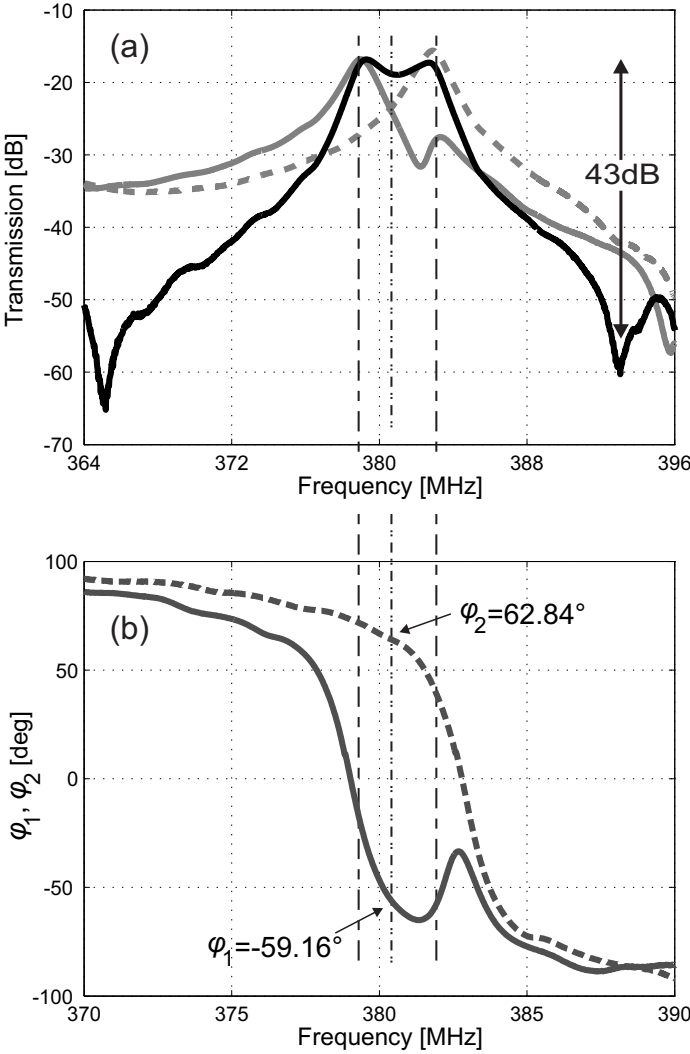


Figure 5.5: (a) The measured transmission of the resonators ( $S_{21}$  and  $S_{43}$ ) and filter ( $S_{dc21}$ ) with  $50\Omega$  termination, (b) The measured phase change of the resonators.

Table 5.1: The resonator performance at DC-bias voltages of 0 and 4 V.

DC-bias [V]	$f_{\text{res1}}$ [MHz]	$R_{\text{m1}}$ [ $\Omega$ ]	$C_{\text{m1}}$ [fF]	$L_{\text{m1}}$ [ $\mu\text{H}$ ]	$\omega_{-3\text{dB}, 1}$ [MHz]	$e_{31, 1}$ [ $\text{C}/\text{m}^2$ ]	$f_{\text{res2}}$ [MHz]	$R_{\text{m2}}$ [ $\Omega$ ]	$C_{\text{m2}}$ [fF]	$L_{\text{m2}}$ [ $\mu\text{H}$ ]	$\omega_{-3\text{dB}, 2}$ [MHz]	$e_{31, 2}$ [ $\text{C}/\text{m}^2$ ]
0	381.7	6410	0.31	574	1.25	-0.61	378.2	6270	0.32	552	1.35	-0.62
4	382.9	542	3.63	47.6	1.8	-2.1	379	631	3.13	56.3	1.8	-1.95

By comparing the measured (Eq. (5.5)) and calculated (Eq. (5.6)) motional impedances, the transverse piezoelectric coefficient ( $e_{31}$ ) of PZT thin-film has been extracted at different DC-bias voltages and listed in Table 5.1. It is illustrated that the absolute value of the  $e_{31}$  is increased from around 0.62 to  $2 \text{ C}/\text{m}^2$  with DC-bias voltage of 0 up to 4 V. The variation of the  $e_{31}$  with the DC-bias voltage is associated with the piezoelectric domain re-orientation process. By applying the DC-bias voltage, the motional impedance is decreasing due to the improvement of the transverse piezoelectric coefficient. The bandwidth of the resonators is increasing which leads to reduction of the ripple. The motional capacitance  $C_{\text{m}}$  and inductance  $L_{\text{m}}$  have been

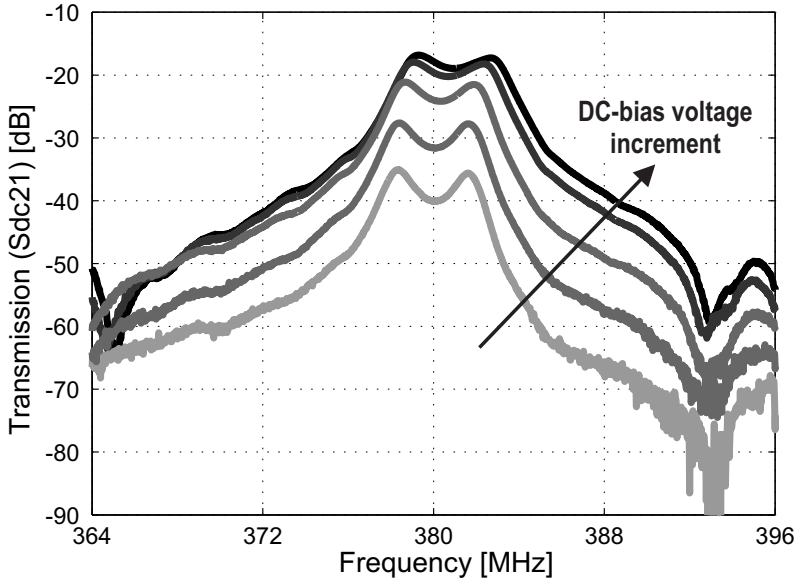


Figure 5.6: Measured transmission gain of the filter at different DC-bias voltages from 0-4 V with 1 V increments.

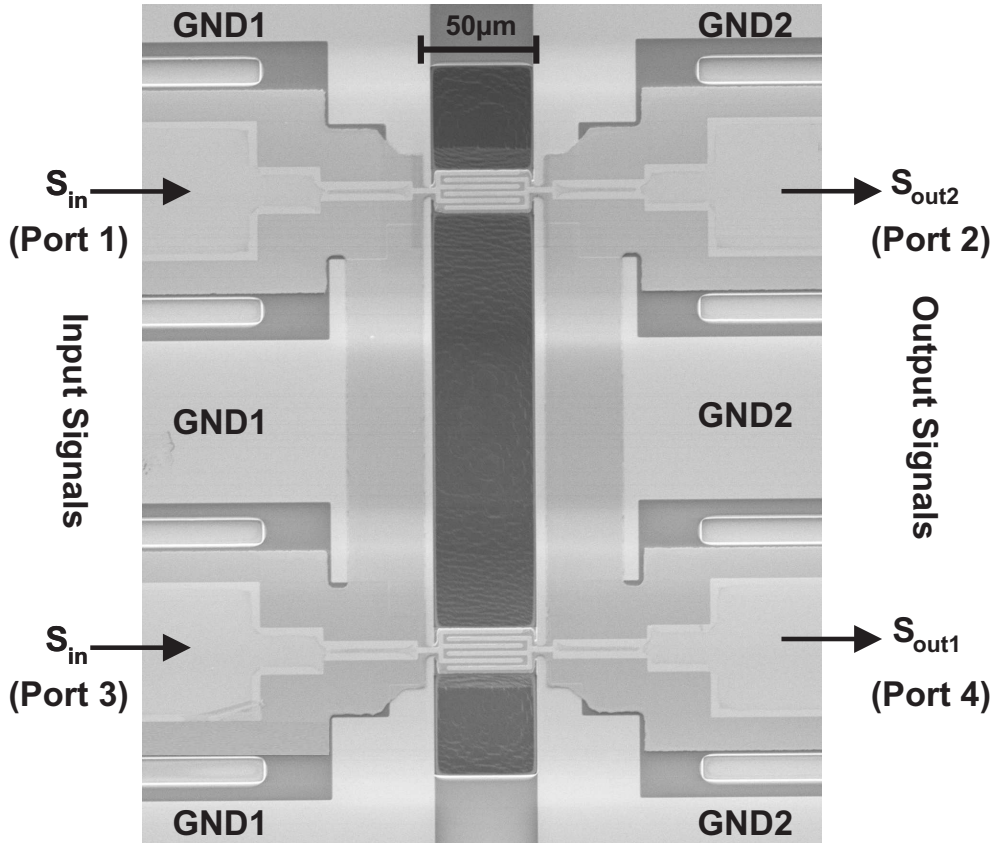


Figure 5.7: Scanning electron micrograph (SEM) of a 4th-order differential readout of in-phase actuated contour-mode PZT-on-silicon filter at 700 MHz.

extracted and reported in Table 5.1. There is also a frequency shift of each resonator of around 1 MHz.

For the second case study, a filter exploiting this technique has been implemented with a center frequency of 700 MHz, illustrated in Fig. 5.7. The BPF is presented using  $50\ \Omega$  termination with bandwidth of approximately 28.6 MHz and 30 dB stopband rejection. All measurements have been done by applying 0 dBm input power. The frequency response of each fabricated resonator ( $S_{21}$  and  $S_{43}$ ) and the differential readout of filter ( $S_{dc21}$ ) at DC-bias voltage of 0 V are shown in Fig. 5.8(a). The phase change of the resonators are presented in Fig. 5.8(b). The phase of the resonator with

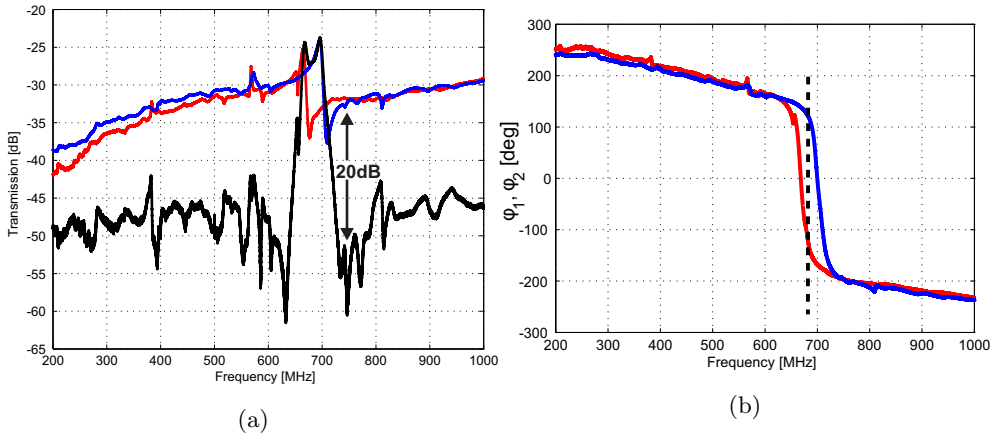


Figure 5.8: (a) Measured transmission gain of individual resonators and the filter (Sdc21) with 50 termination at DC-bias of 0V, (b) The measured phase change of the resonators.

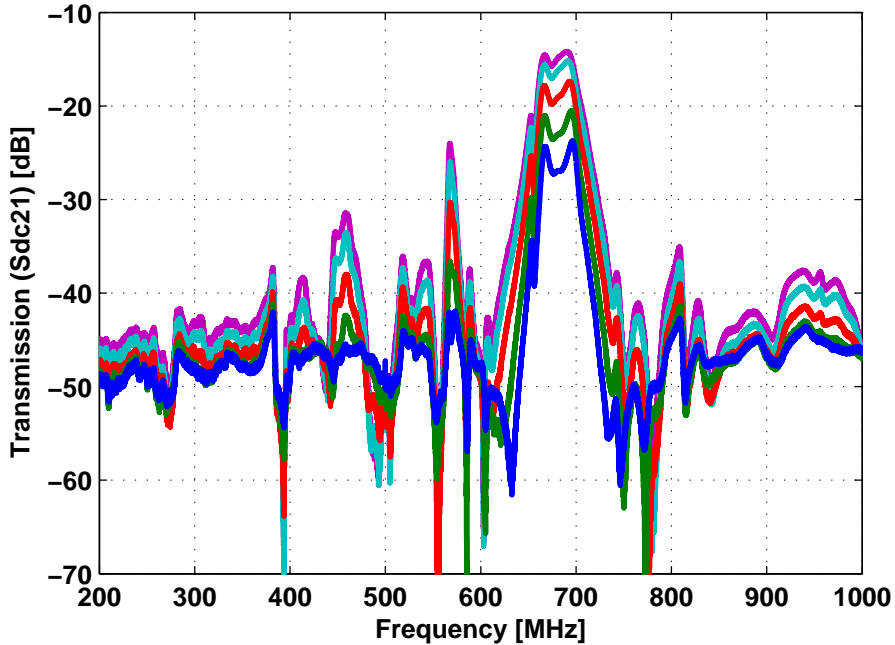


Figure 5.9: Measured transmission gain of the filter at different DC-bias voltages from 0-4 V with 1 V increments.

higher resonance frequency is around  $\varphi_1=120^\circ$  and the lower one is  $\varphi_2=-120^\circ$ . The transmission of filter ( $S_{dc21}$ ) at different DC-bias voltages, 0-4 V, with 1 V increments are presented in Fig. 5.9.

## 5.4 Conclusion

In conclusion, we demonstrated a new 4th-order band-pass filter (BPF) method using the subtraction of two in-phase actuated 2nd-order contour-mode Lamb-wave resonators with slightly different resonance frequencies around 380 MHz and 700 MHz. Utilizing this technique, the output of the resonators are added up constructively as the phase of the resonators are  $\varphi_1 = -\varphi_2$ , while the feed-through signals are eliminated. This technique is a powerful approach for RF-MEMS filter design as well as resolving design issues associated with feed-through at high frequencies for materials with high-dielectric constant such as PZT.



# Chapter 6

## Conclusions

### 6.1 Summary and Conclusion

**In chapter 1**, an introduction and overview of the available RF-MEMS technology was given. Two possible transductions, i.e. capacitive and piezoelectric, were described. Some challenges of RF-MEMS filters and the motivation of this research towards Lamb wave resonators were given. It was described that achieving a high performance multi-band RF-MEMS filter bank in a single fabrication run on the same chip with a reasonable size is a must for next generation wireless communication systems and Lamb wave filters are a suitable candidate to fulfill this demand.

**In chapter 2**, a feed-through cancellation method was proposed. The idea was realized using a length extensional mode resonator. A 250 nm-thick (100)-dominant oriented PZT thin-film deposited on top of 3  $\mu\text{m}$  silicon using pulsed laser deposition (PLD) was employed. The resonator was presented with the length of 40  $\mu\text{m}$  (half-wavelength), which corresponds to a resonance frequency of about 83 MHz. Using the proposed technique, the stopband rejection of the resonator was improved by more than 20 dB. As both input and output ports of RF-MEMS resonators and filter are integrated very close and they are suffering from parasitic capacitance certainly at high frequencies. Therefore, using the proposed technique to de-couple the parasitic capacitances is very important to be able to boost the resonance frequency of RF-MEMS resonators and still keep the rejection floor at lower level.

**In chapter 3**, the feed-through cancellation method was applied for higher-order longitudinal mode resonators which have higher parasitic capacitances due to the

larger areas. Three sets of devices with 1-,  $1\frac{1}{2}$ - and  $2\frac{1}{2}$ -wavelength was presented at resonance frequency around 75 MHz with  $44\ \mu\text{m}$  wavelength using 500 nm-thick pulsed-laser deposited (PLD) lead zirconate titanate (PZT) on top of  $3\ \mu\text{m}$  silicon. Furthermore, the grounding electrodes were separated outside the device to reduce the feed-through signal. A 3D finite element simulation was presented using a fully electro-mechanically coupled models. Finite-element simulation shows a good agreement with the measurement results including an acceptable prediction for the spurious modes. The finite-element simulation approach can be used for future exact designs. The effect of bottom-electrode and ground patternings are showing a coherent behavior on all the sets and providing the opportunity to use a larger size RF-MEMS devices to reduce their motional impedance and therefore their insertion loss.

**In chapter 4**, a bandpass filter using two mechanically coupled contour mode resonators was presented at a resonance frequency of around 380 MHz. The filter was formed of two mechanically-coupled resonators with the same designed wavelength. One resonator was used to actuate the whole coupled structure and the other one was used to pick up the signal. The filter was actuated using two differential input signals and on the other side, the output signal was also picked up using a differential readout. The filter was fabricated using 500 nm-thick pulsed-laser deposited (PLD) lead zirconate titanate (PZT) on top of  $3\ \mu\text{m}$  silicon. The bottom-electrode-patterning technique was applied for the resonators. The filter is characterized using a four-port measurement with  $50\ \Omega$  termination. Using this technique, the filter insertion loss improved around 6 dB as well as the notches of the filter. However, the outside feed-through signals through air and substrate were not eliminated as both actuation and readout were done using a differential technique. Therefore, the filter was showing a low stopband rejection.

**In chapter 5**, a new 4th-order band-pass filter (BPF) method based on differential readout of two in-phase actuated contour-mode Lamb-wave resonators was presented. Two different filters at two different resonance frequencies around 380 MHz and 700 MHz were presented. Each case study was formed of two separate (uncoupled) resonators which had slightly different resonance frequencies. The case study one was presented around 380 MHz and the second case study was presented around 700 MHz. A 500 nm pulsed-laser deposited (PLD) lead zirconate titanate (PZT) thin-film on top of a  $3\ \mu\text{m}$  silicon was used for both filters. The resonators were actuated in-phase and their outputs were subtracted. Utilizing this technique, the feed-through signals were eliminated, while the outputs of the resonators were added up construc-

tively, due to the phase difference between the two output signals. This technique showed a considerable improvement in the performance of RF-MEMS filters compared to the existing Lamb wave filters. Conventional electromechanical filters are using mechanical and/or electrical coupling, however, this new technique is based on the phase change of two un-coupled resonators below and above their resonances. This technique resolves the design issue associated with high feed-through at high frequencies as well as exploiting piezoelectric materials with high-dielectric constant like PZT.

## 6.2 Original Contributions

- A feed-through cancellation method to de-couple the intrinsic parasitic capacitances of 2-port RF-MEMS resonators and filters.
- A fully electro-mechanically coupled simulation of 2-port RF-MEMS resonators for transmission and spurious mode analysis.
- Boosting the resonance frequency of PZT-based bandpass filters exploiting two mechanically coupled Lamb wave resonators and filters.
- Introducing a 4th order bandpass RF-MEMS filter using a differential readout of two un-coupled Lamb wave resonators at the UHF-band and improving the rejection floor by eliminating the feed-through signals.



# Bibliography

- [1] A. Manke, “Crystal Oscillators in Communication Receivers,” *IRE Trans. on Vehicular Communications*, vol. 7, no. 1, pp. 10–15, 1956.
- [2] D. F. Ciccolella and L. J. Labrie, “High Frequency Crystal Units For Use in Selective Networks and Their Proposed Application in Filters Suitable For Mobile Radio Channel Selection,” *Trans. of the IRE Professional Group on Vehicular Communications*, vol. 3, no. 1, pp. 118–128, 1953.
- [3] M. Hikita, T. Tabuchi, and A. Sumioka, “Miniaturized SAW Devices For Radio Communication Transceivers,” *IEEE Trans. on Vehicular Technology*, vol. 38, no. 1, pp. 2–8, 1989.
- [4] C. Campbell, “Applications of Surface Acoustic and Shallow Bulk Acoustic Wave Devices,” *Proceedings of the IEEE*, vol. 77, no. 10, pp. 1453–1484, 1989.
- [5] H. Nathanson, W. Newell, R. Wickstrom, and J. Davis, J.R., “The Resonant Gate Transistor,” *IEEE Trans. on Electron Devices*, vol. 14, no. 3, pp. 117–133, 1967.
- [6] M. Elwenspoek, F. R. Blom, S. Bouwstra, T. Lammerink, F. C. M. Van de Pol, H. A. C. Tilmans, T. J. A. Popma, and J. H. J. Fluitman, “Transduction Mechanisms and Their Applications in Micromechanical Devices,” in *IEEE Micro Electro Mechanical Systems, (MEMS)*, 1989, pp. 126–132.
- [7] W. Tang, T.-C. Nguyen, and R. Howe, “Laterally Driven Polysilicon Resonant Microstructures,” in *IEEE Micro Electro Mechanical Systems (MEMS)*, 1989, pp. 53–59.

- [8] C.-C. Nguyen and R. Howe, "An Integrated CMOS Micromechanical Resonator High-Q Oscillator," *IEEE J. of Solid-State Circuits*, vol. 34, no. 4, pp. 440–455, 1999.
- [9] R. Lifshitz and M. L. Roukes, "Thermoelastic Damping in Micro- and Nanomechanical Systems," *Phys. Rev. B*, vol. 61, pp. 5600–5609, Feb 2000.
- [10] M. Bao and H. Yang, "Squeeze Film Air Damping in MEMS," *Sensors and Actuators A: Physical*, vol. 136, no. 1, pp. 3 – 27, 2007.
- [11] H. Yagubizade and M. I. Younis, "The Effect of Squeeze-Film Damping on the Shock Response of Clamped-Clamped Microbeams," *J. Dyn. Sys., Meas., Control*, vol. 134, no. 1, p. 011017, 2012.
- [12] R. Ruby, P. Bradley, I. Larson, J., Y. Oshmyansky, and D. Figueredo, "Ultra-Miniature High-Q Filters and Duplexers Using FBAR Technology," in *IEEE International Solid-State Circuits Conference (ISSCC), Digest of Technical Papers*, 2001, pp. 120–121.
- [13] C.-C. Nguyen, "MEMS Technology For Timing and Frequency Control," *IEEE Trans. on Ultrasonics, Ferroelectrics and Frequency Control*, vol. 54, no. 2, pp. 251–270, 2007.
- [14] R. Abdolvand, H. Lavasani, G. Ho, and F. Ayazi, "Thin-Film Piezoelectric-on-Silicon Resonators For High-Frequency Reference Oscillator Applications," *IEEE Trans. on Ultrasonics, Ferroelectrics and Frequency Control*, vol. 55, no. 12, pp. 2596–2606, 2008.
- [15] K. Wang and C.-C. Nguyen, "High-Order Medium Frequency Micromechanical Electronic Filters," *J. of Microelectromechanical Systems*, vol. 8, no. 4, pp. 534–556, 1999.
- [16] F. Bannon, J. Clark, and C.-C. Nguyen, "High-Q HF Microelectromechanical Filters," *IEEE J. of Solid-State Circuits*, vol. 35, no. 4, pp. 512–526, 2000.
- [17] A.-C. Wong and C.-C. Nguyen, "Micromechanical Mixer-Filters ("Mixlers")," *J. of Microelectromechanical Systems*, vol. 13, no. 1, pp. 100–112, 2004.
- [18] Y.-W. Lin, S. Lee, S.-S. Li, Y. Xie, Z. Ren, and C.-C. Nguyen, "Series-Resonant VHF Micromechanical Resonator Reference Oscillators," *IEEE J. of Solid-State Circuits*, vol. 39, no. 12, pp. 2477–2491, 2004.

- 
- [19] J. Wang, Z. Ren, and C.-C. Nguyen, "1.156-GHz Self-Aligned Vibrating Micromechanical Disk Resonator," *IEEE Trans. on Ultrasonics, Ferroelectrics and Frequency Control*, vol. 51, no. 12, pp. 1607–1628, 2004.
- [20] J. Clark, W.-T. Hsu, M. Abdelmoneum, and C.-C. Nguyen, "High-Q UHF Micromechanical Radial-Contour Mode Disk Resonators," *J. of Microelectromechanical Systems*, vol. 14, no. 6, pp. 1298–1310, 2005.
- [21] S. Lee and C.-C. Nguyen, "Mechanically-Coupled Micromechanical Resonator Arrays For Improved Phase Noise," in *Proceedings of IEEE International Frequency Control Symposium and Exposition*, 2004, pp. 144–150.
- [22] Y.-W. Lin, S.-S. Li, Y. Xie, Z. Ren, and C.-C. Nguyen, "Vibrating Micromechanical Resonators With Solid Dielectric Capacitive Transducer Gaps," in *Proceedings of IEEE International Frequency Control Symposium and Exposition*, 2005, pp. 128–134.
- [23] Y.-W. Lin, S.-S. Li, Z. Ren, and C.-C. Nguyen, "Third-Order Intermodulation Distortion in Capacitively-Driven VHF Micromechanical Resonators," in *IEEE Ultrasonics Symposium*, vol. 3, 2005, pp. 1592–1595.
- [24] C.-C. Nguyen and J. Kitching, "Towards Chip-Scale Atomic Clocks," in *IEEE International Solid-State Circuits Conference, (ISSCC), Digest of Technical Papers*, 2005, pp. 84–85.
- [25] Y. Xie, S.-S. Li, Y.-W. Lin, Z. Ren, and C.-C. Nguyen, "UHF Micromechanical Extensional Wine-Glass Mode Ring Resonators," in *IEEE International Electron Devices Meeting, IEDM '03 Technical Digest.*, 2003, pp. 39.2.1–39.2.4.
- [26] C.-C. Nguyen, "Vibrating RF MEMS For Next Generation Wireless Applications," in *Proceedings of the IEEE Custom Integrated Circuits Conference*, 2004, pp. 257–264.
- [27] —, "Integrated Micromechanical Circuits for RF Front Ends," in *Proceedings of the 32nd European Solid-State Circuits Conference (ESSCIRC)*, 2006, pp. 7–16.
- [28] —, "6I-4 Integrated Micromechanical Circuits Fueled By Vibrating RF MEMS Technology (Invited)," in *IEEE Ultrasonics Symposium*, 2006, pp. 957–966.

- [29] S.-S. Li, Y.-W. Lin, Z. Ren, and C.-C. Nguyen, "An MSI Micromechanical Differential Disk-Array Filter," in *International Solid-State Sensors, Actuators and Microsystems Conference (TRANSDUCERS)*, 2007, pp. 307–311.
- [30] Y.-W. Lin, L.-W. Hung, S.-S. Li, Z. Ren, and C.-C. Nguyen, "Quality Factor Boosting via Mechanically-Coupled Arraying," in *International Solid-State Sensors, Actuators and Microsystems Conference (TRANSDUCERS)*, 2007, pp. 2453–2456.
- [31] M. Abdelmoneum, M. Demirci, and C.-C. Nguyen, "Stemless Wine-Glass-Mode Disk Micromechanical Resonators," in *IEEE International Conference on Micro Electro Mechanical Systems (MEMS)*, 2003, pp. 698–701.
- [32] T. Cheng and S. Bhawe, "High-Q, Low Impedance Polysilicon Resonators With 10 nm Air Gaps," in *IEEE 23rd International Conference on Micro Electro Mechanical Systems (MEMS)*, 2010, pp. 695–698.
- [33] D. Weinstein and S. Bhawe, "Internal Dielectric Transduction in Bulk-Mode Resonators," *J. of Microelectromechanical Systems*, vol. 18, no. 6, pp. 1401–1408, 2009.
- [34] —, "Internal Dielectric Transduction of a 4.5 GHz Silicon Bar Resonator," in *IEEE International Electron Devices Meeting (IEDM)*, 2007, pp. 415–418.
- [35] H. Chandrahali, D. Weinstein, L. F. Cheow, and S. Bhawe, "Channel-Select Micromechanical Filters Using High-K Dielectrically Transduced MEMS Resonators," in *IEEE International Conference on Micro Electro Mechanical Systems (MEMS) Istanbul*, 2006, pp. 894–897.
- [36] H. Chandrahali, D. Weinstein, L. F. Cheow, and S. A. Bhawe, "High-k Dielectrically Transduced MEMS Thickness Shear Mode Resonators and Tunable Channel-Select RF Filters," *Sensors and Actuators A: Physical*, vol. 136, no. 2, pp. 527–539, 2007.
- [37] V. Yantchev and I. Katardjiev, "Thin Film Lamb Wave Resonators in Frequency Control and Sensing Applications: A Review," *J. of Micromechanics and Microengineering*, vol. 23, no. 4, p. 043001, 2013.
- [38] J. Bjurström, I. Katardjiev, and V. Yantchev, "Lateral-Field-Excited Thin-Film Lamb Wave Resonator," *Applied Physics Letters*, vol. 86, no. 15, p. 154103, 2005.

- 
- [39] P. Stephanou and A. Pisano, "GHZ Contour Extensional Mode Aluminum Nitride MEMS Resonators," in *IEEE Ultrasonics Symposium*, 2006, pp. 2401–2404.
- [40] C. Zuo, J. Van der Spiegel, and G. Piazza, "1.05-GHz CMOS Oscillator Based on Lateral-Field-Excited Piezoelectric AlN Contour-Mode MEMS Resonators," *IEEE Trans. on Ultrasonics, Ferroelectrics and Frequency Control*, vol. 57, no. 1, pp. 82–87, 2010.
- [41] G. Piazza, P. Stephanou, and A. Pisano, "Piezoelectric Aluminum Nitride Vibrating Contour-Mode MEMS Resonators," *J. of Microelectromechanical Systems*, vol. 15, no. 6, pp. 1406–1418, 2006.
- [42] M. Rinaldi, C. Zuo, J. Van der Spiegel, and G. Piazza, "Reconfigurable CMOS Oscillator Based on Multifrequency AlN Contour-Mode MEMS Resonators," *IEEE Trans. on Electron Devices*, vol. 58, no. 5, pp. 1281–1286, 2011.
- [43] J. Kuypers and A. Pisano, "Green's Function Analysis of Lamb Wave Resonators," in *IEEE Ultrasonics Symposium*, 2008, pp. 1548–1551.
- [44] V. Yantchev, "Zero Mass Loading Sensitivity of the S0 Lamb Wave Resonance in Thin Film Plate Acoustic Resonators (FPARs)," in *IEEE Ultrasonics Symposium*, 2009, pp. 2181–2184.
- [45] C. Zuo and G. Piazza, "Single-Ended-to-Differential and Differential-to-Differential Channel-Select Filters Based on Piezoelectric AlN Contour-Mode MEMS Resonators," in *IEEE International Frequency Control Symposium (FCS)*, 2010, pp. 5–8.
- [46] M. Rinaldi, C. Zuniga, and G. Piazza, "Ultra-Thin-Film AlN Contour-Mode Resonators For Sensing Applications," in *IEEE International Ultrasonics Symposium*, 2009, pp. 714–717.
- [47] H. Chandrahali, S. Bhave, R. Polcawich, J. Pulskamp, and R. Kaul, "PZT Transduction of High-Overtone Contour-Mode Resonators," *IEEE Trans. on Ultrasonics, Ferroelectrics and Frequency Control*, vol. 57, no. 9, pp. 2035–2041, 2010.
- [48] H. Yagubizade, M. Darvishi, M. C. Elwenspoek, and N. R. Tas, "A 4th-Order Band-Pass Filter Using Differential Readout of Two In-Phase Actuated Contour-Mode Resonators," *Applied Physics Letters*, vol. 103, no. 17, p. 173517, 2013.

- [49] P. Stephanou, G. Piazza, C. D. White, M. Wijesundara, and A. Pisano, "Mechanically Coupled Contour Mode Piezoelectric Aluminum Nitride MEMS Filters," in *IEEE International Conference on Micro Electro Mechanical Systems (MEMS) Istanbul*, 2006, pp. 906–909.
- [50] C. Perez and G. Piazza, "Bandwidth Control in Acoustically Coupled AlN Contour Mode MEMS Filters," in *IEEE International Frequency Control Symposium, Joint with the 22nd European Frequency and Time forum.*, 2009, pp. 64–69.
- [51] H. Chandrahali, S. Bhave, R. Polcawich, J. Pulskamp, and R. Kaul, "A Pb(Zr<sub>0.55</sub>Ti<sub>0.45</sub>)O<sub>3</sub>-Transduced Fully Differential Mechanically Coupled Frequency Agile Filter," *IEEE Electron Device Letters*, vol. 30, no. 12, pp. 1296–1298, 2009.
- [52] G. Piazza, P. Stephanou, and A. Pisano, "Single-Chip Multiple-Frequency ALN MEMS Filters Based on Contour-Mode Piezoelectric Resonators," *J. of Microelectromechanical Systems*, vol. 16, no. 2, pp. 319–328, 2007.
- [53] H. Chandrahali, S. Bhave, R. Polcawich, J. Pulskamp, D. Judy, R. Kaul, and M. Dubey, "Performance Comparison of Pb(Zr<sub>0.55</sub>Ti<sub>0.45</sub>)O<sub>3</sub>-Only and Pb(Zr<sub>0.55</sub>Ti<sub>0.45</sub>)O<sub>3</sub>-on-Silicon Resonators," *Applied Physics Letters*, vol. 93, no. 23, p. 233504, 2008.
- [54] G. Ho, R. Abdolvand, A. Sivapurapu, S. Humad, and F. Ayazi, "Piezoelectric-on-Silicon Lateral Bulk Acoustic Wave Micromechanical Resonators," *J. of Microelectromechanical Systems*, vol. 17, no. 2, pp. 512–520, 2008.
- [55] C.-M. Lin, Y.-Y. Chen, V. V. Felmetger, D. G. Senesky, and A. P. Pisano, "AlN/3CSiC Composite Plate Enabling High-Frequency and High-Q Micromechanical Resonators," *Advanced Materials*, vol. 24, no. 20, pp. 2722–2727, 2012.
- [56] S. Gong, N.-K. Kuo, and G. Piazza, "GHz High-Q Lateral Overmoded Bulk Acoustic-Wave Resonators Using Epitaxial SiC Thin Film," *J. of Microelectromechanical Systems*, vol. 21, no. 2, pp. 253–255, 2012.
- [57] T. Manzanque, V. Ruiz, J. Hernando-Garcia, A. Ababneh, H. Seidel, and J. Sanchez-Rojas, "Characterization and Simulation of the First Extensional Mode of Rectangular Micro-plates in Liquid Media," *Applied Physics Letters*, vol. 101, no. 15, p. 151904, 2012.

- 
- [58] G. L. Smith, J. S. Pulskamp, L. M. Sanchez, D. M. Potrepka, R. M. Proie, T. G. Ivanov, R. Q. Rudy, W. D. Nothwang, S. S. Bedair, C. D. Meyer, and R. G. Polcawich, "PZT-Based Piezoelectric MEMS Technology," *J. of the American Ceramic Society*, vol. 95, no. 6, pp. 1777–1792, 2012.
- [59] M. D. Nguyen, M. Dekkers, E. Houwman, R. Steenwelle, X. Wan, A. Roelofs, T. Schmitz-Kempen, and G. Rijnders, "Misfit Strain Dependence of Ferroelectric and Piezoelectric Properties of Clamped (001) Epitaxial  $\text{Pb}(\text{Zr}_{0.55}, \text{Ti}_{0.45})\text{O}_3$  thin films," *Applied Physics Letters*, vol. 99, no. 25, p. 252904, 2011.
- [60] S. S. Bedair, D. Judy, J. Pulskamp, R. G. Polcawich, A. Gillon, E. Hwang, and S. Bhave, "High Rejection, Tunable Parallel Resonance in Micromachined Lead Zirconate Titanate on Silicon Resonators," *Applied Physics Letters*, vol. 99, no. 10, p. 103509, 2011.
- [61] J. Pulskamp, S. Bedair, R. Polcawich, D. Judy, and S. Bhave, "Ferroelectric PZT RF MEMS Resonators," in *Joint Conference of the IEEE International Frequency Control and the European Frequency and Time Forum (FCS)*, 2011, pp. 1–6.
- [62] M. Dekkers, H. Boschker, M. van Zalk, M. Nguyen, H. Nazeer, E. Houwman, and G. Rijnders, "The Significance of the Piezoelectric Coefficient  $d_{31,\text{eff}}$  Determined From Cantilever Structures," *J. of Micromechanics and Microengineering*, vol. 23, no. 2, p. 025008, 2013.
- [63] C. Ayela, L. Nicu, C. Soyer, E. Cattan, and C. Bergaud, "Determination of the  $d_{31}$  Piezoelectric Coefficient of  $\text{PbZr}_x\text{Ti}_{1-x}\text{O}_3$  thin films using multilayer buckled micromembranes," *J. of Applied Physics*, vol. 100, no. 5, p. 054908, 2006.
- [64] C. Zuo, N. Sinha, and G. Piazza, "Very High Frequency Channel-Select MEMS Filters Based on Self-Coupled Piezoelectric AlN Contour-Mode Resonators," *Sensors and Actuators A: Physical*, vol. 160, no. 12, pp. 132 – 140, 2010.
- [65] S. Tallur and S. A. Bhave, "A Silicon Electromechanical Photodetector," *Nano Letters*, vol. 13, no. 6, pp. 2760–2765, 2013.
- [66] H. Fatemi and R. Abdolvand, "High-Frequency Thin-Film Piezoelectric Transformers," in *IEEE International Frequency Control Symposium (FCS)*, 2012, pp. 1–4.

- [67] S. Bedair, J. Pulskamp, R. Polcawich, B. Morgan, J. Martin, and B. Power, "Thin-Film Piezoelectric-on-Silicon Resonant Transformers," *J. of Microelectromechanical Systems*, vol. PP, no. 99, pp. 1–1, 2013.
- [68] S. Bedair, J. Pulskamp, R. Polcawich, D. Judy, A. Gillon, S. Bhave, and B. Morgan, "Low Loss Micromachined Lead Zirconate Titanate Contour Mode Resonator With  $50 \Omega$  Termination," in *IEEE 25th International Conference on Micro Electro Mechanical Systems (MEMS)*, 2012, pp. 708–712.
- [69] B. P. Harrington and R. Abdolvand, "In-Plane Acoustic Reflectors For Reducing Effective Anchor Loss in Lateral Extensional MEMS Resonators," *J. of Micromechanics and Microengineering*, vol. 21, no. 8, p. 085021, 2011.
- [70] H. Fatemi, H. Zeng, J. Carlisle, and R. Abdolvand, "High-Frequency Thin-Film AlN-on-Diamond Lateral-Extensional Resonators," *J of Microelectromechanical Systems*, vol. 22, no. 3, pp. 678–686, 2013.
- [71] T.-T. Yen, A. Pisano, and C.-C. Nguyen, "High-Q Capacitive-Piezoelectric AlN Lamb Wave Resonators," in *IEEE 26th International Conference on Micro Electro Mechanical Systems (MEMS)*, 2013, pp. 114–117.
- [72] J. Pulskamp, S. Bedair, R. Polcawich, G. Smith, J. Martin, B. Power, and S. Bhave, "Electrode-Shaping For the Excitation and Detection of Permitted Arbitrary Modes in Arbitrary Geometries in Piezoelectric Resonators," *IEEE Trans. on Ultrasonics, Ferroelectrics and Frequency Control*, vol. 59, no. 5, pp. 1043–1060, 2012.
- [73] C.-M. Lin, Y.-J. Lai, J.-C. Hsu, Y.-Y. Chen, D. G. Senesky, and A. P. Pisano, "High-Q Aluminum Nitride Lamb Wave Resonators With Biconvex Edges," *Applied Physics Letters*, vol. 99, no. 14, pp. –, 2011.
- [74] H. Yagubizade, M. Darvishi, Y.-Y. Chen, M. D. Nguyen, J. M. Dekkers, R. J. Wiegerink, M. C. Elwenspoek, and N. R. Tas, "Pulsed-Laser Deposited Pb(Zr<sub>0.55</sub>, Ti<sub>0.45</sub>)O<sub>3</sub>-on-Silicon Resonators With High-Stopband Rejection Using Feed-Through Cancellation," *Applied Physics Letters*, vol. 102, no. 6, p. 063509, 2013.
- [75] I. Larson, J.D., S. Gilbert, and B. Xu, "PZT Material Properties at UHF and Microwave Frequencies Derived From FBAR Measurements," in *IEEE Ultrasonics Symposium (IUS)*, vol. 1, 2004, pp. 173–177.

- [76] S. Gong and G. Piazza, “Design and Analysis of Lithium-Niobate-Based High Electromechanical Coupling RF-MEMS Resonators for Wideband Filtering,” *IEEE Trans. on Microwave Theory and Techniques*, vol. 61, no. 1, pp. 403–414, 2013.
- [77] R. Wang, S. Bhawe, and K. Bhattacharjee, “High  $k_t^2Q$ , Multi-frequency Lithium Niobate Resonators,” in *IEEE 26th International Conference on Micro Electro Mechanical Systems (MEMS)*, 2013, pp. 165–168.



# Acknowledgement

Everybody starts a PhD with a great passion to discover something unique which at least will overturn the field. By the passage of time, you start to realize that it is other way around and PhD is overturning you. The only thing which keeps you continuing is bringing the expectations down. This is the only way to be able to concentrate and find out the way to continue. This was the most important thing that I learned during my PhD.

When I was doing my master thesis, I have found a lot of great works done about micro-resonators by former PhD students of Prof. Miko Elwenspoek. Indeed, they did a great work back on those days. It was at the end of my master thesis that all of a sudden I noticed a PhD vacancy about nano-resonators in TST group, called CREAM project. I thought if they did such a great work twenty five years ago, then imagine how good they are now. This was my main motivation to apply for this position. After starting my PhD, I noticed those researches were the last works on MEMS resonators done by TST and RF-MEMS field is not the main topic of the group. At the beginning, I was more guided towards nano-fabrication to use silicon nanowire resonators which resonate at high frequencies, however, we found out that it was not a good solution. Afterward, together with Dr. Niels Tas, we started to discover RF-MEMS field using piezoelectric transduction. Fortunately, we found out our own way and even presented some new ideas in the field. Niels, Thanks for all your support.

I enjoyed the few discussions I had with Dr. Remco Wiegerink about analyzing high-frequency resonators and how to tackle the feed-through signals. The CREAM project was in collaboration with ICD and SC groups. Due to this collaboration, I worked closely with Milad (ICD group) and Naveed (SC group). We had different backgrounds (electrical engineering, physics and mechanical engineering) and at the beginning, we had difficulties to understand each other. However, by the passage

of time we started to understand the terms we were using for the same thing. Due to this collaboration, I learned a lot from other fields, mainly electrical engineering aspects in RF-MEMS. With Milad we started to find new ideas and publish several papers together. Thank you Milad and Naveed. During this work, I did collaboration with SolMateS (a spin-off company at UT). I would like to thank Dr. Minh Nguyen and Dr. Matthijn Dekkers as well as Prof. Guus Rijnders for sharing their expertise and providing PZT thin-films. I did all my measurements in ICD group with the help of Henk de Vries. I would like to thank Erwin and Meint for helping me in the fabrication and designing the fabrication process flows. This project was funded by STW (Dutch Technology Foundation). I would like to thank all the user committee members for attending to the meetings and their comments.

My special thanks go to Marcel. We had a great time and discussions on different topics. I was lucky that you were also working in the evenings. Thanks for your company and sharing all your experiences. I would like to thank Maarten for being patient during the time I was working till late night and was not able to join for dinner and shopping, etc. That was my pleasure to be your housemate. I would like to thank all the former and current TST members that I had the chance to work with. Thanks for providing such a nice environment. Thank you all.

I would like to thank all my friends for being with me in all the times as well as having fun all together. Unfortunately it is not possible to mention all the memories and the name of the people who have touched my life in the past years. Therefore I would like to thank you all for being with me.

I consider myself lucky that I had a great supervisor, Prof. Gh. Rezazadeh, during my master studies who introduced me to the MEMS world. Thanks for the time and efforts you have invested in me. I would like to thank Prof. M.I. Younis for his great support during my master studies and his guidance. I would also like to thank Prof. H. Motavalli who always encouraged me to keep continuing my education.

I would like to thank my parents and my brother, for their endless support and their encouragement in all the stages of my life. Finally, but foremost, I would like to thank Shirin, my wife, for her full accompaniment and patience during the period we were far from each other. It was so hard to be separated after visiting you just for few weeks within a whole year. I wish this will not happen again and we will be together forever.

Hadi Yagubizade  
Enschede, December 2013

# Samenvatting

Draadloze communicatie systemen omvatten tegenwoordig tal van standaarden waar voor bijna elke standaard een andere frequentieband is toegewezen. Met de toename in draadloze apparatuur dreigt het radio spectrum overvol te raken, wat leidt tot een groeiende vraag naar slimme, “cognitieve” radio apparatuur, welke ongebruikte delen van het spectrum kunnen detecteren en benutten. Dit vertaalt zich naar de wens voor een radio systeem met een groot frequentiebereik, van ongeveer 50 MHz tot 5 GHz. Een belangrijke eis hiervoor is het realiseren van een programmeerbare RF pre-filter bank, bestaande uit meerdere RF filters van verschillende frequenties.

Een RF filter bank vereist vergaande miniaturisatie omdat de huidige filters (bijvoorbeeld surface acoustic wave of film-bulk akoestische resonatoren) groot zijn en moeilijk te integreren in grote aantallen op verschillende frequenties. Ondanks een decennium aan onderzoek in dit onderwerp, zijn geventureerde hoge-kwaliteits bandpass filter banken nog steeds niet gerealiseerd. Daarom gebruiken de hedendaagse draadloze systemen meestal individuele filters buiten de chip, in plaats van volledig geventureerde bandpass filters.

Piezoelektrisch vibrerende componenten zijn geëvolueerd tot een nieuwe klasse van apparaten zoals surface acoustic wave (SAW) en bulk acoustic wave (BAW) resonatoren en filters met hoge werkingsfrequenties. Nieuwe micro-fabricage technieken zoals ontwikkeld voor de IC industrie hebben massafabricage van deze apparaten met kleinere afmetingen en lagere kosten mogelijk gemaakt. Deze apparaten consumeren echter nog steeds het overgrote deel van het circuitoppervlak en ze kunnen niet makkelijk gefabriceerd worden op hetzelfde substraat. Bij SAW filters penetreren de mechanische trillingen het piezoelektrische substraat, waardoor de afmetingen groot moeten blijven om de motionele impedantie laag te houden.

BAW filters (bijv. FBAR) daarentegen gebruiken dunne-film piezoelektrische materialen, maar hun resonantiefrequentie is afhankelijk van de laagdikte. Hierdoor is het

rendabel maken van een BAW filter bank een grote uitdaging. Lamb-golf piezoelektrische RF-MEMS resonatoren en filters zijn erg interessant geworden omdat hun resonantiefrequentie afhangt van de laterale afmetingen van de elektrodes en omdat ze van het substraat gescheiden zijn, waardoor ze een hoge Q-factor krijgen. Hierdoor zijn Lamb-golf filters de beste kandidaat om SAW en BAW filters te vervangen.

Lamb-golf piezoelektrische RF-MEMS resonatoren hebben veelbelovende eigenschappen getoond, zoals lage ingangsimpedantie en hoge Q-factor. Hun Q-factor is vergroot door ze te integreren met eenkristallijne materialen als eenkristal silicium of siliciumcarbide, welke in elke cyclus energie opslaan en afgeven met minder verlies dan een piezoelektrisch medium. Lamb-golf resonatoren zijn ook erg interessant voor zeer gevoelige sensoren vanwege hun hoge Q-factor. Lamb-golf resonatoren zijn nog in de optimalisatiefase, dus er is grote vraag naar betere oplossingen voor het verminderen van ankerverlies, onechte modi onderdrukking door ontwerpvariaties, en simulatietechnieken zoals eindige elementen methoden.

AlN, ZnO en recentelijk PZT dunne films zijn de meestgebruikte piezoelektrische materialen in de resonatoren. PZT heeft hiervan de hoogste elektromechanische koppelingsfactor wat een groot voordeel is voor het verminderen van de filterafmetingen en het laag houden van de ingangsimpedantie. PZT heeft echter een lagere fasesnelheid, wat het moeilijk maakt om erg hoge resonantiefrequenties te bereiken. Hogere netto fasesnelheden kunnen in PZT bereikt worden in combinatie met andere materialen met hogere fasesnelheden (bijvoorbeeld silicium).

PZT heeft last van een hoge feed-through vanwege zijn hoge dielektrische permittiviteit, waardoor de stopband verzwakking sterk afneemt. In dit proefschrift introduceren wij een methode voor het opheffen van deze feed-through, bij aanwezigheid van imperfecte aarding aan de input en output kanalen welke in praktische situaties onontkoombaar is door de weerstanden naar aarde. Deze aardingsweerstand zijn specifiek meegenomen in de ontwerpen. Met de voorgestelde methode is de stopband verzwakking van de resonator met meer dan 20 dB verbeterd.

Twee verschillende bandpass filter configuraties (mechanisch gekoppeld en differentiele uitlezing) worden in dit proefschrift beschreven. Het mechanisch gekoppelde filter bestaat uit twee mechanisch gekoppelde resonatoren met dezelfde bepaalde golflengte. Een resonator wordt gebruikt om de gekoppelde structuur te actueren en de andere wordt gebruikt om het signaal op te nemen. Het mechanisch gekoppelde filter wordt geactueerd met twee differentiele ingangssignalen en uitgelezen met twee differentiele uitgangssignalen.

---

Omdat zowel de actuatie als de uitlezing met een differentiele techniek uitgevoerd zijn, worden de feed-through signalen door lucht en substraat niet volledig tegengegaan. Hierdoor toont het filter een lage stopband verzwakking. Om dit probleem te verhelpen wordt een nieuw concept voor bandpass filters voorgesteld in dit proefschrift, genaamd differentiele uitlezings-filter. Twee verschillende filters met twee verschillende resonantiefrequenties rond de 370 MHz en 700 MHz worden gepresenteerd. Deze techniek biedt een aanzienlijke verbetering in prestaties van RF-MEMS filters vergeleken met de bestaande Lamb-golf filters. Gebruikelijke elektromechanische filters maken gebruik van mechanische en/of elektrische koppeling, terwijl de nieuwe techniek gebaseerd is op de faseverandering van twee ongekoppelde resonatoren onder en boven hun resonantie. Deze techniek biedt een oplossing voor het ontwerpprobleem van hoge feed-through bij hoge frequenties, en maakt daarnaast gebruik van piezoelectrische materialen met hoge dielectrische constantes, zoals PZT.



# Abstract

Nowadays, wireless communication systems cover numerous standards where almost for each one, a different frequency band has been allocated. By increasing the number of wireless devices, the radio spectrum is quickly becoming overcrowded, asking for smart “cognitive radio” devices, which detect and exploit unused spectrum. This means that a radio system which can cover a wide frequency range from about 50 MHz to 5 GHz is desirable. A key roadblock in this respect is the realization of programmable RF pre-filter bank which contains several RF filters operating at different frequency bands. An RF filter bank requires miniaturization as the current filters (i.e. surface acoustic wave and film-bulk acoustic resonators) are big and it is not easy to integrate several of them together at different frequency bands. Up till now, it was not possible to build integrated high-performance bandpass filter bank despite more than a decade of research on this topic. For this reason, nowadays, most wireless systems utilize individual off-chip filters rather than fully integrated bandpass filters. This increases the size and the cost. Therefore, considerable research is going on for launching a technology, that enables implementation of all the required frequency-selective components on a single substrate that eventually will be integrated into the electronic circuit.

Piezoelectric vibrating components have evolved into new classes of devices such as surface acoustic wave (SAW) and bulk acoustic wave (BAW) resonators and filters with high operational frequencies. Novel micro-fabrication techniques developed for IC industry created opportunities for batch fabrication of these devices in smaller size at lower cost. However, they still consume far more area than the rest of the electronic circuit and can not be easily fabricated on the same substrate. SAW filters are bulky devices and the mechanical waves are penetrating to the piezoelectric substrate. Therefore, the size of SAW filters are big to keep the motional impedance low. On the other hand, BAW filters (e.g. FBAR) use thin-film piezoelectric materi-

als, but their resonance frequencies are thickness dependent. Therefore, fabricating a BAW filter bank is not cost effective and is a big challenge. Lamb-wave piezoelectric RF-MEMS resonators and filters became a very interesting topic as their resonance frequency depends on the lateral dimensions of the electrodes and they are released from substrate, providing a high  $Q$ -factor performance. Therefore, Lamb wave filters are the best candidate for replacing of SAW and BAW filters.

Lamb-wave piezoelectric RF-MEMS resonators have demonstrated promising performance, such as low motional impedance and high  $Q$ -factor. Their  $Q$ -factor has been boosted by integrating them with single crystalline materials, e.g. single-crystalline silicon and silicon carbide, which store energy and deliver it back in each cycle with less loss compared to the piezoelectric medium. Also Lamb-wave resonators are of great interest for highly sensitive sensors due to their high  $Q$ -factor. Lamb-wave resonators are still in the perfecting state and therefore there is a great demand for further understanding of various issues such as reducing the anchor-loss, spurious mode suppression using various designs and simulation techniques such as finite-element methods.

AlN, ZnO and recently PZT thin-films are the prevalent piezoelectric materials utilized in the resonators. Of these, PZT has the highest electromechanical coupling-factor which is a big opportunity to reduce the size of the filters and keep the motional impedance low. However, PZT has a lower phase velocity, which makes it difficult to achieve very-high resonance frequencies. Higher composite phase velocities can be obtained by PZT in combination with other materials having higher phase velocities (e.g. silicon). PZT suffers from a high feed-through due to its high dielectric permittivity which, as a consequence, drastically reduces the stopband rejection. In this thesis, to overcome this problem, we propose a feed-through cancellation method in the presence of specific grounding resistances (non-zero grounding) at the input- and output-sides, which always exist and prevent perfect grounding. Particularly, these grounding resistances have been considered in the designs. Using the proposed technique, the stopband rejection of the resonator is improved by more than 20 dB.

Two different bandpass filter configurations (i.e. mechanically coupled and differentially readout) are presented in this thesis. The mechanically-coupled filter consists of two mechanically-coupled resonators with identical designed wave-length. One resonator is used to actuate the whole coupled structure and the other one is used to pick up the signal. The mechanically-coupled filter is actuated using two differential input signals and on the other side, the output signal is also picked up using a differential

---

readout. As both actuation and readout are done using a differential technique, the feed-through signals through air and substrate are not eliminated. Therefore, the filter shows a low stopband rejection. To overcome this problem, a new concept of bandpass filter is proposed in this thesis called, differential readout filter. Two different filters at two different resonance frequencies around 380 MHz and 700 MHz are presented. This technique showed a considerable improvement in the performance of RF-MEMS filters compared to the existing Lamb wave filters. Conventional electromechanical filters are using mechanical and/or electrical couplings, however, this new technique is based on the phase change of two un-coupled resonators below and above their resonances. This technique resolves the design issue associated with high feed-through at high frequencies as well as exploiting piezoelectric materials with high-dielectric constant like PZT.



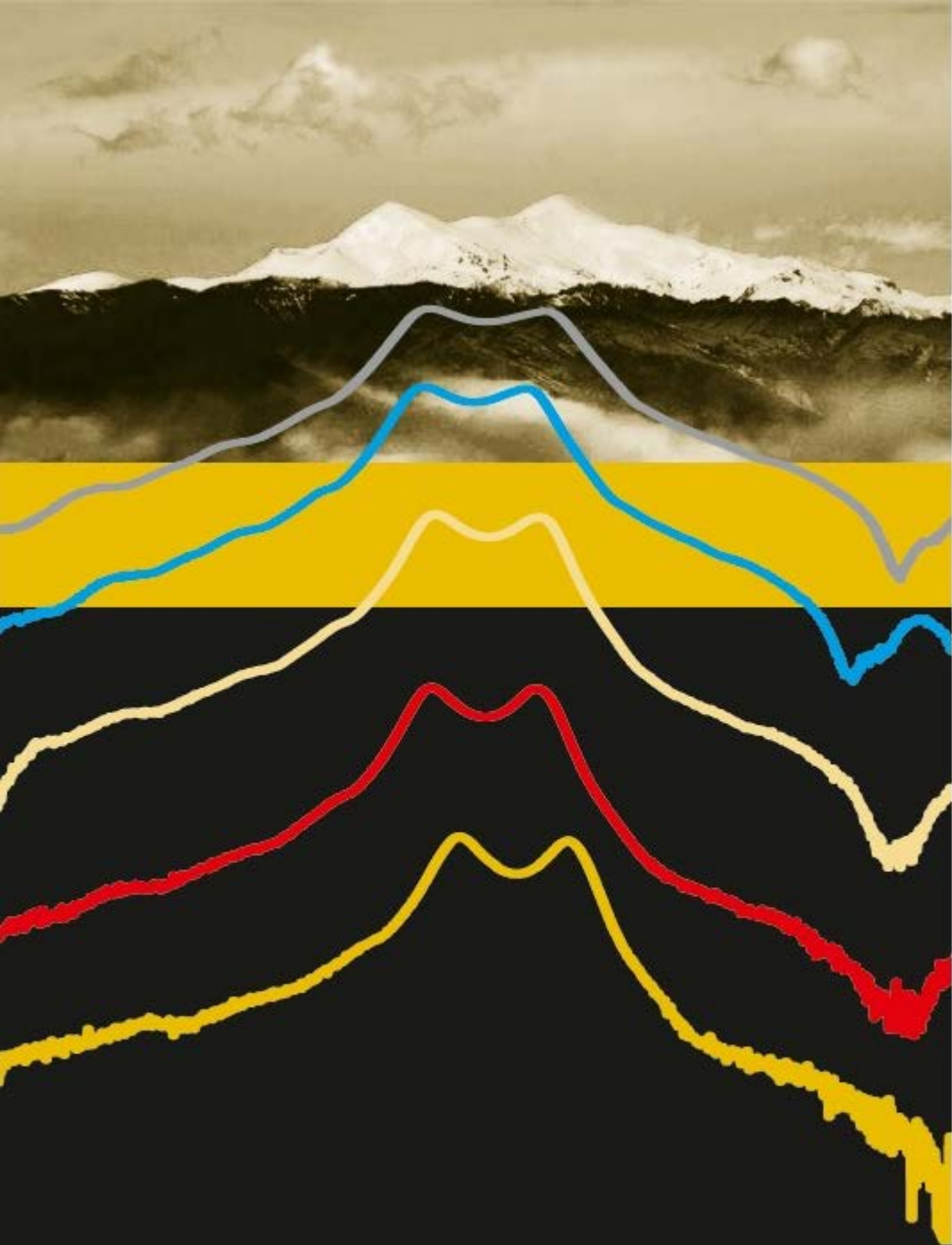
# List of Publications

- [1] **H. Yagubizade**, M. Darvishi, M. C. Elwenspoek, and N. R. Tas, “A 4th-Order Band-Pass Filter Using Differential Readout of Two In-phase Actuated Contour-Mode Resonators,” *Applied Physics Letters*, vol. 103(17), 173517, 2013.
- [2] **H. Yagubizade**, M. Darvishi, Y.-Y. Chen, M. D. Nguyen, J. M. Dekkers, R. J. Wiegink, M. C. Elwenspoek, and N. R. Tas, “Pulsed-Laser Deposited Pb(Zr<sub>0.55</sub>Ti<sub>0.45</sub>)O<sub>3</sub>-on-Silicon Resonators with High-stopband Rejection Using Feed-Through Cancellation,” *Applied Physics Letters*, vol. 102(6), 063509, 2013.
- [3] **H. Yagubizade**, M. Darvishi, M. C. Elwenspoek, and N. R. Tas, “A UHF 4th-Order Bandpass Filter Based on Contour-Mode PZT-on-Silicon Resonators,” *IEEE Micro Electro Mechanical Systems, (MEMS)*, Jan. 2014.
- [4] **H. Yagubizade**, M. Darvishi, Y.-Y. Chen, M. D. Nguyen, J. M. Dekkers, R. J. Wiegink, M. C. Elwenspoek, and N. R. Tas, “Higher-Order Longitudinal Mode PZT-on-Silicon Resonators: Bottom-Electrode and Ground Patterning,” Submitted to *J. Micromechanics and Microengineering*, 2013.
- [5] **H. Yagubizade** and M. I. Younis, “The Effect of Squeeze-Film Damping on the Shock Response of Clamped-Clamped Microbeams,” *J. of Dynamic Systems, Measurement and Control, Trans. of the ASME*, 134(1), 011017, 2012.
- [6] S.M.C. Abdulla, **H. Yagubizade**, and G. J. M. Krijnen, “Analysis of Resonance Frequency and Pull-in Voltages of Curled Micro-Bimorph Cantilevers,” *J. of Micromechanics and Microengineering* 22(3), 035014, 2012.

- [7] E. Berenschot, **H. Yagubizade**, H. V. Jansen, M. Dijkstra, and N. R. Tas, "Fabrication of 2D-Extruded Fractal Structures Using Repeated Corner Lithography and Etching," *IEEE NEMS conf.*, April. 2014.
- [8] **H. Yagubizade**, E. Berenschot, H. V. Jansen, M. Elwenspoek, and N. R. Tas, "Silicon Nanowire Fabrication Using Edge and Corner Lithography," *IEEE Nanotechnology Materials and Devices Conference (NMDC2010)*, 5652181, pp. 128-131.
- [9] O.S. Sukas, **H. Yagubizade**, J. W. Berenschot, M. J. de Boer, M. D. Nguyen, L. Abelman, "Characterization of Piezoelectrically Actuated PLD Pb(Zr,Ti)O<sub>3</sub> Thin Film Membranes," *23rd Micromechanics and Microsystems Europe Workshop (MME 2012)*, Sep. 2012.
- [10] **H. Yagubizade**, M. I. Younis, and Gh. Rezazadeh, "The Effect of Squeeze-Film Damping on Suppressing the Shock Response of MEMS," *Proc. ASME., Micro and Nano Systems* 12(303), Jan. 2009.

# Biography

**Hadi Yagubzade** received B.S. and M.Sc. degrees in Mechanical Engineering from Urmia University in 2006 and 2008, respectively. His master thesis was about fluid-structure interaction (FSI) of MEMS structures under electrostatic and mechanical shock loads. In January 2009, he joined University of Twente as a PhD student in Transducers Science and Technology (TST) Group at MESA<sup>+</sup> Institute for Nanotechnology. His Ph.D. project was about high-frequency Lamb wave MEMS resonators and filters using piezoelectric transduction. His current research interests include RF-MEMS bandpass filters and acousto-microfluidics. He is an author and co-author of more than 10 papers.



ISBN 978-90-365-3594-6